The Astrophysical Journal Supplement Series, 173:143–165, 2007 November

AN IMAGING SURVEY FOR EXTRASOLAR PLANETS AROUND 45 CLOSE, YOUNG STARS WITH THE SIMULTANEOUS DIFFERENTIAL IMAGER AT THE VERY LARGE TELESCOPE AND MMT[1]

Beth A. Biller,[1] Laird M. Close,[1] Elena Masciadri,[2] Eric Nielsen,[1] Rainer Lenzen,[3] Wolfgang Brandner,[3]
Donald McCarthy,[1] Markus Hartung,[4,5] Stephan Kellner,[6] Eric Mamajek,[7] Thomas Henning,[3]
Douglas Miller,[1] Matthew Kenworthy,[1] and Craig Kulesa[1]

Received 2007 January 23; accepted 2007 April 23

ABSTRACT

We present the results of a survey of 45 young ($\lesssim$250 Myr), close ($\lesssim$50 pc) stars with the Simultaneous Differential Imager (SDI) implemented at the VLT and the MMT for the direct detection of extrasolar planets. As part of the survey, we observed 54 objects, consisting of 45 close, young stars; two more distant (<150 pc), extremely young ($\leq$10 Myr) stars; three stars with known radial velocity planets; and four older, very nearby ($\leq$20 pc) solar analogs. Our SDI devices use a double Wollaston prism and a quad filter to take images simultaneously at three wavelengths surrounding the 1.62 μm methane absorption bandhead found in the spectrum of cool brown dwarfs and gas giant planets. By differencing adaptive optics–corrected images in these filters, speckle noise from the primary star is significantly attenuated, resulting in photon (and flat-field)–noise–limited data. In our VLT data, we achieved *H*-band contrasts $\gtrsim$10 mag (5 σ) at a separation of 0.5″ from the primary star on 45% of our targets and *H*-band contrasts $\gtrsim$ 9 mag at a separation of 0.5″ on 80% of our targets. With these contrasts, we can image (5 σ detection) a 7 M_J planet 15 AU from a 70 Myr K1 star at 15 pc or a 7.8 M_J planet at 2 AU from a 12 Myr M star at 10 pc. We detected no candidates with S/N > 2 σ which behaved consistently like a real object. From our survey null result, we can rule out (with 93% confidence) a model planet population where $N(a) \propto$ constant out to a distance of 45 AU.

Subject headings: instrumentation: adaptive optics — planetary systems

Online material: color figure

1. INTRODUCTION

While over 200 extrasolar planets have been detected[8] over the last 11 years (mostly via the radial velocity technique), very few extrasolar planet candidates have been imaged directly (for instance, 2MASS 1207b [$\sim$8 ± 3 M_J], Oph 1622B [$\sim$13 ± 5 M_J], and CHXR 73B [$\sim$12.5 ± 8 M_J]; Chauvin et al. 2005a; Close et al. 2007a; Luhman et al. 2006; Brandeker et al. 2006). The few candidates discovered of "planetary mass" <13 M_J are companions to brown dwarfs and possess properties more similar to young brown dwarfs (separations > 50 AU; surface gravity $g \gtrsim 0.3$) than to giant extrasolar planets orbiting Sun-like stars. Based on their large (>50 AU) separations, these objects appear to have formed via a fragmentation process, more similar to that which formed brown dwarfs. Hence, to date no true images of extrasolar planets have been obtained.

Theoretically, a large telescope (D > 6 m) plus an adaptive optics (AO) system should be able to reach the photon-noise limit at 1″ separations from the star with an hour of exposure time and thus attain the very high (>10^5) contrasts necessary to image a young extrasolar giant planet. Thus, numerous AO surveys to directly detect extrasolar planets have been completed (for instance, Kaisler et al. 2003; Masciadri et al. 2005). These surveys have yielded interesting contrast limits but no true extrasolar giant planet candidates.

The difficulty in directly imaging extrasolar giant planets can be attributed to the unfortunate fact that bright quasi-static speckles (also known as superspeckles) caused by slowly evolving instrumental aberrations remain in AO images even after AO correction (see, for example, Racine et al. 1999). These superspeckles evolve stochastically on relatively long (minute) timescales and also vary somewhat chromatically, producing correlated speckle noise which is very difficult to calibrate and remove (Racine et al. 1999). For photon-noise-limited data, the signal-to-noise ratio (S/N) increases as $t^{0.5}$, where t is the exposure time. Approximately speaking, for speckle-noise-limited data, the S/N does not increase with time past a specific speckle-noise floor (limiting AO contrasts often to $\sim 10^3$ at 0.5″; Racine et al. 1999; Masciadri et al. 2005). More exactly, S/N does continue to increase with time, but as the speckle noise in successive frames becomes correlated, the N gain becomes considerably slower. Effectively independent exposures then have durations of many minutes rather than a small fraction of a second (Racine et al. 1999). This correlated speckle noise is considerably above the photon-noise limit and makes planet detection very difficult. Interestingly, space telescopes such as *Hubble Space Telescope* (*HST*) also suffer from limiting correlated speckle noise due to temperature variations which induce changes in the point-spread function (PSF) (known as "breathing"; G. Schneider et al. 2003, unpublished).

Many observatories, including Gemini, Subaru, and the Very Large Telescope (VLT), are currently building dedicated planet-finding AO/coronagraph cameras in order to overcome this speckle-noise floor (Dohlen et al. 2006; Macintosh et al. 2006; Tamura &

---

[1] Steward Observatory, University of Arizona, Tucson, AZ 85721.

[2] Observatorio Astrofisico di Arcetri, Largo Enrico Fermi 5, 50125 Florence, Italy.

[3] Max-Planck-Institut für Astronomie, Königstuhl 17, 69117 Heidelberg, Germany.

[4] European Southern Observatory, Alonso de Cordova 3107, Santiago 19, Chile.

[5] Departamento de Astronomía, Universidad de Chile, Casilla 36-D, Santiago, Chile.

[6] W. M. Keck Observatory, 65-1120 Mamalahoa Highway, Kamuela, HI 96743.

[7] Harvard-Smithsonian Center for Astrophysics, 60 Garden Street, Cambridge, MA 02138.

[8] http://exoplanet.eu/catalog.php, maintained by Jean Schneider.

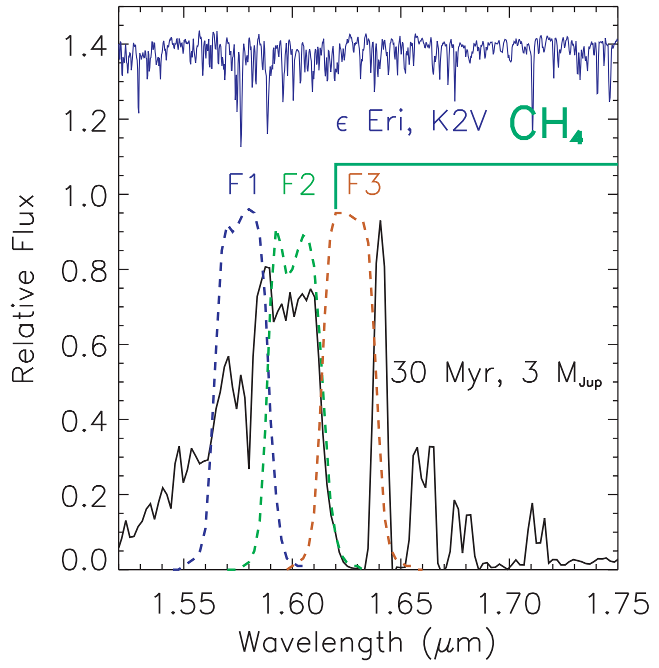

Fig. 1.—SDI filter transmission curves overlaid on the theoretical spectrum (D. Sudarsky 2004, private communication) of a young extrasolar planet (30 Myr, 3 M_J). Filters 1 and 2 sample off the 1.62 μm CH_4 absorption feature, while filter 3 samples within the absorption feature. In contrast, the spectrum of the K2 V star ϵ Eri (Meyer et al. 1998) is flat across the whole wavelength band. Subtracting images taken in filters "on" and "off" the methane absorption feature will remove the star and speckle noise (which is coherent with the starlight) while preserving any light from giant planet companions. (Details of the complex SDI data pipeline are provided in § 2.3.)

Lyu 2006). A number of instrumental speckle-attenuation methods have been proposed, such as spectral differential imaging (Racine et al. 1999; Marois et al. 2000a, 2000b, 2005), azimuthal differential imaging (Marois et al. 2006), integral-field spectroscopy (Sparks & Ford 2002; Berton et al. 2006; Thatte et al. 2007), precise wavelength control methods such as those developed at the High Contrast Imaging Testbed (Trauger et al. 2004), focal plane wave front sensing (Codona & Angel 2004; Kenworthy et al. 2006), and nulling interferometry (Liu et al. 2007).

The Simultaneous Differential Imagers (SDIs) at the VLT and MMT, built and commissioned by our team (Lenzen et al. 2004, 2005; Close et al. 2005a), use a spectral differential speckle-attenuation technique (pioneered by Racine et al. 1999; Marois et al. 2000a, 2000b, 2005). It exploits a methane absorption feature at 1.62 μm (see Fig. 1) which is robustly observed in substellar objects with spectral type later than T3.5 (Geballe et al. 2002; Burrows et al. 2001). SDI uses specialized hardware to image simultaneously inside and outside this methane feature with custom 25 nm filters (see Fig. 1). Since the superspeckles are coherent with the starlight and both starlight and speckles have a flat spectrum (see Fig. 1) in this narrow wavelength band ($\delta\lambda/\lambda \simeq 1.6\%$), subtracting the "on" and "off" methane absorption images removes the starlight and its speckles, while preserving light from any substellar methane companion to the star.

We have completed a 54 star survey with the SDI device at the VLT and MMT. Survey stars were chosen primarily according to proximity to the Sun ($\lesssim$50 pc) and youth ($\lesssim$300 Myr, typically $<$100 Myr). We observed 47 young ($\lesssim$250 Myr) stars, three nearby stars with known radial velocity planets, and four very close ($\lesssim$20 pc) older solar analogs. We obtained contrasts of $\Delta H > 10$ mag ($5\ \sigma$) at $0.5''$ for 45% of target objects at the VLT and contrasts of $\Delta H > 9$ mag ($5\ \sigma$) at $0.5''$ for 80% of our targets. The VLT SDI device is fully commissioned and available to the community, and the MMT SDI device is a PI instrument with the ARIES camera. In contrast, the dedicated planet-finding instruments such as Sphere and Gemini Planet Imager (Dohlen et al. 2006; Macintosh et al. 2006) being built at the VLT and Gemini, respectively, will not see first light for several years. Thus, as a precursor to planet surveys with these dedicated planet-finding cameras, the results from the SDI devices are especially timely and relevant, particularly to inform the large Gemini Near-Infrared Coronagraphic Imager survey starting in 2007 (M. Liu et al. 2005, unpublished).

2. THE SIMULTANEOUS DIFFERENTIAL IMAGERS AT THE VLT AND MMT

The VLT SDI was built at the University of Arizona by L. M. C. and installed in a special f/40 camera relay for the VLT AO camera CONICA built by R. L. at the Max Planck Institute for Astronomy, in Heidelberg, Germany (Lenzen et al. 2003; Rousset et al. 2003). These were both installed at the VLT in 2003 August. The MMT SDI was also built at the University of Arizona. In 2004 February, it was installed in the ARIES f/30 camera built by D. M. Both devices are available to the observing communities of their respective telescopes.

2.1. *Hardware Considerations*

The SDI device consists of a custom double Wollaston, which splits the incoming AO beam into four identical beams (using calcite birefringence to minimize noncommon path error—adding only $\lesssim$10 nm rms of differential noncommon path errors per the first few Zernike modes; Lenzen et al. 2004). Each beam then passes through a narrowband filter with a central wavelength either on or off the methane absorption. Three different filters were used; all filters were placed in different quadrants on the same substrate. SDI filters for the VLT and MMT were manufactured by Barr Associates. Filter wavelengths were chosen on and off the methane absorption feature at 1.62 μm and were spaced closely (every 0.025 μm) in order to limit residuals due to speckle and calcite chromatism. We used four filters F1, F2, F3a, and F3b with measured cold central wavelengths F1 $\equiv$ 1.575 μm, F2 $\equiv$ 1.600 μm, and F3a $\equiv$ F3b $\equiv$ 1.625 μm. The filters are approximately 0.025 μm in bandwidth (1.6%). The SDI filter transmission curves overlaid on a theoretical young planet spectrum (D. Sudarsky 2004, private communication) are presented in Figure 1.

2.2. *Discoveries with the SDI Cameras*

The SDI device has already produced a number of important scientific results: the discovery of the important calibrator object AB Dor C (Close et al. 2005b) which is the tightest ($0.16''$) low-mass ($0.090 \pm 0.05\ M_{\odot}$, $\sim$100 times fainter) companion detected by direct imaging; the most detailed methane surface maps of Titan from the pre-*Cassini* era (Hartung et al. 2004); the discovery of ϵ Ind Ba and Bb, the nearest binary brown dwarf (McCaughrean et al. 2004); the discovery of SCR 1845−6357B, a very close (3.85 pc) T6 brown dwarf (Biller et al. 2006b); and evidence of orbital motion for Gl 86B, the first known white dwarf companion to an exoplanet host star (Mugrauer & Neuhäuser 2005). In fact, the SDI device discovered all known brown dwarfs within 5 pc of the Sun. It has also set the best upper limit on the luminosity of the older ($\sim$1 Gyr) extrasolar planet around ϵ Eri.

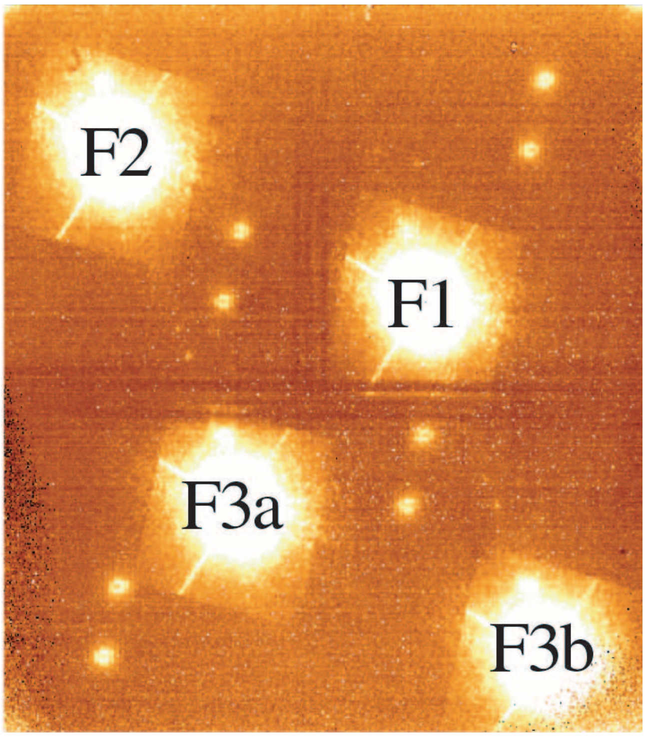

Fig. 2.—Two minutes of raw SDI data from NACO SDI's 1024 × 1024 Aladdin array in the VLT CONICA AO camera (Lenzen et al. 2004). A number of electronic ghosts are apparent outside the four square filter apertures (each aperture is rotated by 30°); indeed, filter apertures were specifically selected to exclude these ghosts. Note that this is an image of the original Alladin array; the current SDI array has far fewer bad pixels.

2.3. *Observational Techniques and Data Reduction*

To ensure the highest possible S/N and to maximize SDI speckle attenuation, a complex data acquisition procedure was followed for each star. For each object observed, we saturated the inner ~0.1″ of the star, thus providing a wide dynamic range and contrast down into the halo. Base exposure times (DIT) range from 0.3 to 20 s (typically this was >2 s to allow Fowler sampling at the VLT), depending on the *H* magnitude of the observed star. A number of exposures (NDIT) with the base exposure time are then co-added in hardware to produce a standard ~2 minute long base datum. An example raw datum is presented in Figure 2.[9]

Base datum are then taken at a grid of dither positions (4 × 0.5″ spacings with the MMT, 5 × 0.5″ spacings with the VLT). This dither pattern is then repeated at typically two telescope "roll angles" (where a "roll angle" refers to a different field derotator position/position angle [PA] settings). A subtraction of data taken at different roll angles further attenuates superspeckle residuals (since the weak residual speckles after SDI subtraction are instrumental features in the SDI optics which do not shift with a change in roll angle) while producing a very important signature "jump" in position for any physical companion (since a physical companion will appear to shift by the roll angle difference between data sets). For a space telescope such as *HST* (where the entire telescope can be rolled), a companion detected at the 5 σ level in two different roll angles would be detected at the 7 σ level (a S/N gain of $\sim\sqrt{2}$) across the entire data set (assuming roughly Gaussian statistics). This method is somewhat less effective with ground-based telescopes where field rotation is provided by the field derotator rather than rolling the entire telescope (thus, superspeckles from the telescope optics can appear to rotate by the roll angle as well). Nonetheless, observing at two roll angles provides us with two independent detections of a substellar companion at different locations on the detector, thus allowing us to rule out a "false positive" detection at an extremely high level of confidence: indeed, the only three faint companions (ϵ Ind Bb, SCR 1845−6357B, and AB Dor C) ever detected with $\geq$5 σ using SDI in more than one roll angle have *all proven to be real*. A typical observing block at the VLT then consists of the following series of (1) a ~10 minute long dither pattern taken with a roll angle of 0°, (2) a ~10 minute long dither pattern taken with a roll angle of 33°, (3) a ~10 minute long dither pattern taken with a roll angle of 33°, and (4) a ~10 minute long dither pattern taken with a roll angle of 0°. A custom template was developed at the VLT to automate this process in each observation block.

Each base datum was reduced using a custom IDL pipeline (described in detail in Biller et al. 2006a, 2006c). This pipeline performs sky subtraction, flat fielding, and bad pixel removal, extracts a square aperture around each separate filter image, scales the plate scale of each filter image so that the speckles in each filter fall at the same radii despite chromatic differences, scales the flux in each image to remove any quantum efficiency differences between the images, and filters out very low (>15 pixels) spatial frequencies by unsharp masking each image. Each filter image is then initially aligned to a reference image to within 0.25 pixels using a custom shift and subtract algorithm (Biller et al. 2006a, 2006c). One master reference image is used for each ~40 minute long data set. After each of the filter images has been aligned to the reference image, we calculate two differences which are sensitive to substellar companions of spectral types T ($T_{\rm eff} < 1200$ K) and "Y" ($T_{\rm eff} < 600$ K). The first is optimal for T spectral types:

$$\text{Difference1} = \text{F1}(1.575\ \mu\text{m}) - \text{F3a}(1.625\ \mu\text{m}). \qquad (1)$$

The second is optimal for Y spectral types:

$$\text{Difference2} = \text{F2}(1.6\ \mu\text{m}) - \text{F3a}(1.625\ \mu\text{m}). \qquad (2)$$

An additional alignment is performed before the SDI subtraction; using the F1 image as our reference image, we align images F1 and F3a to within 0.05 pixels. A similar alignment is performed with images F2 and F3a, using the F2 image as the reference image.

These differences are also somewhat sensitive to hotter substellar companions (L and early T spectral types), due to the fact that the plate scale in each filter image has been scaled to a reference plate scale to align the Airy patterns in each image. A real object (as opposed to a speckle) will not scale with the Airy pattern and thus, after scaling, will appear at a slightly different radius in each filter image. Subtracting images in different filters will then produce a characteristic dark-light radial pattern for a real object. This effect obviously scales with radius; at the VLT, an object at 0.5″ will be offset by less than 1 pixel between filters, while an object at 1.5″ will be offset by ~3 pixels, producing a very noticeable pattern. Thus, the SDI subtractions have a limited sensitivity to bright L and early T companions. We note that AB Dor C ($\Delta H \sim 5$ mag) was detected at 0.15″ (2004 February; Close et al. 2005b) and 0.2″ (2004 September; Nielsen et al. 2005) separations from AB Dor A even though AB Dor C has no methane

---

[9] As with all our survey data, this was taken with the original SDI double Wollaston prism. In 2007 February, the original prism was replaced with a next-generation prism which is cut in such a way that each subimage now subtends a whole quadrant of the detector chip. The new prism is also fabricated from YV04, a material which produces smaller chromatic errors at 1.6 μm than the original calcite.

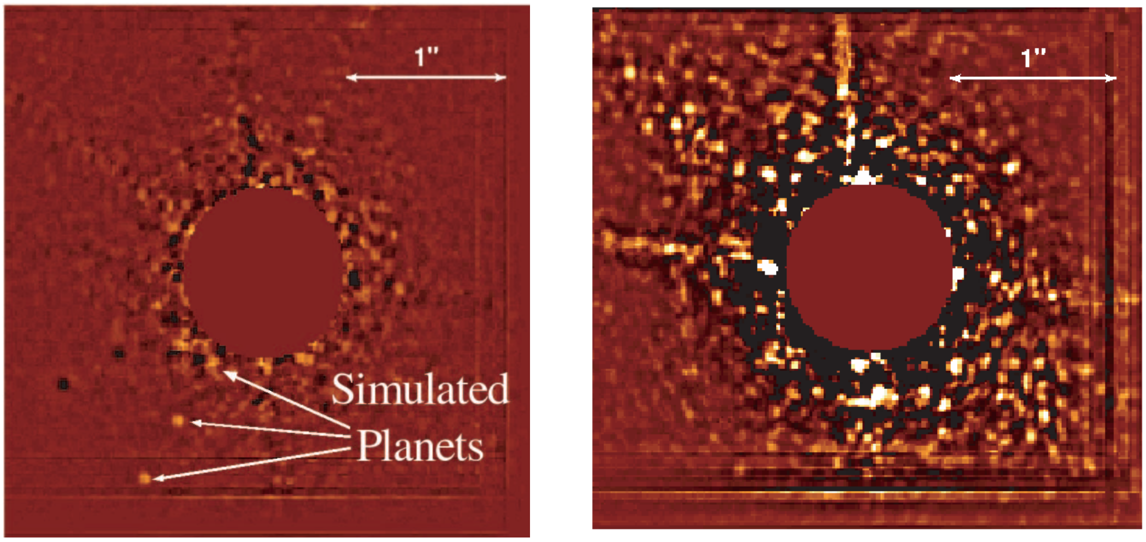

FIG. 3.—*Left*: Complete reduced data set (28 minutes of data at a series of rotator angles ["roll angles"]: 0°, 33°, 33°, 0°) from the VLT SDI device. Simulated planets have been added at separations of 0.55″, 0.85″, and 1.35″ from the primary, with ΔF1(1.575 μm) = 10 mag (star-planet contrast) fainter than the primary. These planets are scaled from unsaturated images of the example star (AB Dor A) taken right before the example data set (and have fluxes and photon noise in each filter appropriate for a T6 effective temperature). Past 0.7″, the simulated planets are detected in both roll angles with S/N > 10. Observing at two different roll angles produces two independent detections and hence makes the chance of detecting a "false positive" almost null. *Right*: Standard AO data reduction of the same data set. Filter images have been co-added (rather than subtracted), flat-fielded, sky-subtracted, and unsharp-masked. Simulated planets have been added with the same properties and at the same separations as before. None of the simulated planets are clearly detected in the standard AO reduction. In addition, many more bright superspeckles remain in the field.

absorption features (as is expected from its M5.5 spectral type; Close et al. 2007b.)

We additionally calculate one further nondifferenced combination sensitive to M, L, and early T companions:

$$\begin{aligned}\text{Broadband} = {} & \text{F1}(1.575\ \mu\text{m}) \\ & + \text{F2}(1.6\ \mu\text{m}) + \text{F3}(1.625\ \mu\text{m}) \qquad (3)\end{aligned}$$

After each datum is pipelined the data are further processed in IRAF. For each ~10 minute long dither pattern, all three combinations described above and the four reduced filter images are median combined. Each 10 minute data set is then differenced with the following 10 minute data set (taken at a different PA). All roll-angle differenced images for each target object observation are then median combined to produce the final data product.

A fully reduced ~30 minute data set of AB Dor A (70 Myr K1 V star at a distance of 14.98 pc, $V = 6.88$) from the VLT SDI device is presented in Figure 3. Simulated planets have been added at separations of 0.55, 0.85, and 1.35″ from the primary, with ΔF1(1.575 μm) = 10 mag (attenuation in magnitudes in the 1.575 μm F1 filter) fainter than the primary. For details and further discussion of these planet simulations see § 3.4.

3. THE SDI SURVEY

3.1. *Survey Design/Target Selection*

Survey objects were selected primarily on the basis of youth and proximity. With a number of exceptions, our 54 survey objects are within 50 pc of the Sun and less than 250 Myr in age. (The nine exceptions include three somewhat older stars with known radial velocity planets, two more distant [<150 pc] stars with extreme youth indicators, and four older nearby young solar analogs which were initially misclassified as young objects.) Distances were obtained for 48 of our objects from *Hipparcos* parallax measurements (parallaxes of >0.02″, corresponding to distances < 50 pc; Perryman et al. 1997). Stars were age-selected according to two methods: (1) if possible, according to young cluster membership (and adopting the established age for that cluster) for clusters with well established ages such as the β Pic, TW Hya, AB Dor, and Tuc-Hor moving groups or (2) according to other age indicators including the strength of spectral age indicators

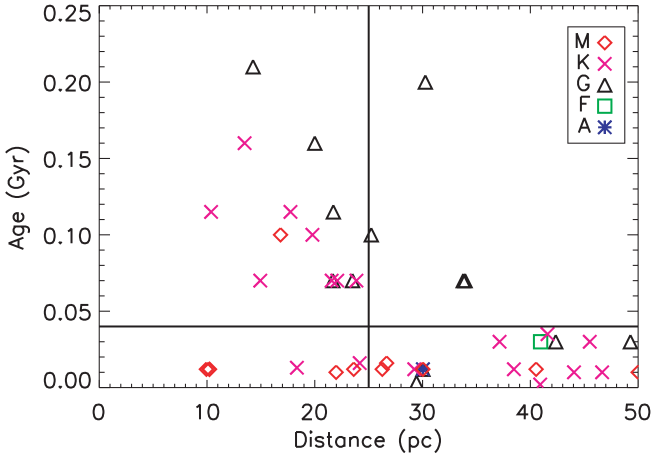

FIG. 4.—Age vs. distance for our survey stars. Spectral types are delineated by plot symbols. Objects were selected according to youth and proximity to the Sun. Forty-five of our survey objects are within 50 pc of the Sun and less than 250 Myr in age. Of the remaining objects, two are very young (<10 Myr), somewhat more distant (<150 pc) objects; three are nearby stars with known radial velocity planets; and four are nearby solar analogs (<20 pc) that were initially misclassified as young. We selected targets according to two overlapping criteria (*solid black lines*) (1) stars within 25 pc and younger than 250 Myr and (2) stars within 50 pc and younger than 40 Myr. Stars were age-selected according to association membership, or, in the case of unassociated stars, age indicators such as the strength of the Li λ6707 line, Ca H and K lines, Hα emission, X-ray emission, etc. Distances were obtained from *Hipparcos* parallax measurements (parallaxes of >0.02″). Our "median" survey object is a K star with an age of 30 Myr and at a distance of 25 pc.

TABLE 1
Properties of SDI Survey Stars

Target	R.A.[a] (J2000.0)	Decl. (J2000.0)	Distance (pc)[a]	SpT[b]	SpT Ref.	Age (Gyr)[c]	Age Ref.[c]	V[d]	H[e]	Detectability	Comments
Nearby Young Stars											
HIP 1481	00 18 26.1	−63 28 39.0	41	F8/G0 V	1	0.03	Tuc	7.5	6.2	2.0%	
ERX6	01 23 21.2	−57 28 50.7	49.3	G6 V	1	0.03	Tuc/Hor	8.5	6.9	2.4%	
ERX8	01 28 08.7	−52 38 19.2	37.1	K1 V	1	0.03	Tuc/Hor	9.3	6.9	7.2%	
HIP 9141	01 57 48.9	−21 54 05.0	42.4	G3 Ve/G5 V	2	0.03	Tuc/Hor	8.1	6.6	2.0%	Poss. 0.15″ binary
BD +05 378	02 41 25.9	+05 59 18.4	40.5	M0	3	0.012	β Pic	10	7.2	3.4%	
HD 17925	02 52 32.1	−12 46 11.0	10.4	K1 V	2	0.115	Possible Her/Lyr	6	4.2	8.4%	
LH 98 062	03 24 06.5	+23 47 06.1	19.8	K4 V	4	0.1	Li from LH98	10	6.5		2.4″ binary
V577 PerA	03 33 13.5	+46 15 26.5	33.8	G5 IV/V	5	0.07	AB Dor mg	8.3	6.5	2.0%	7″ binary
V834 Tau	04 41 18.9	+20 54 05.4	13.5	K3 V	6	0.16	Li from W03	8.1	5.3	4.0%	
GJ 182	04 59 34.8	+01 47 00.7	26.7	M1 Ve	7	0.016	Li from F97	10	6.5	8.7%	Very tentative planet candidate (4.8 AU, $\sim$4 $M_{\rm J}$) not detected at second epoch
HIP 23309	05 00 47.1	−57 15 25.5	26.3	M0/1	8	0.012	β Pic	10	6.4	11%	
AB Dor	05 28 44.8	−65 26 54.9	14.9	K1 III	1	0.07	AB Dor mg	6.9	4.8	9.0%	0.16″ binary AB Dor C (Close et al. 2005a)
GJ 207.1	05 33 44.8	+01 56 43.4	16.8	M2.5e	9	0.1	L05	9.5	7.1	5.7%	
UY Pic	05 36 56.8	−47 57 52.9	23.9	K0 V	10	0.07	AB Dor mg	8	5.9	9.6%	
AO Men	06 18 28.2	−72 02 41.4	38.5	K6/7	8	0.012	β Pic	9.9	7	0.2%	Very tentative planet candidate (14 AU, $\sim$4 $M_{\rm J}$) not detected at second epoch
HIP 30030	06 19 08.1	−03 26 20.0	52.4	G0 V	11	0.03	Tuc/Hor	8	6.6	0%	
AB Pic	06 19 12.9	−58 03 16.0	45.5	K2 V	1	0.03	Tuc	9.1	7.1	5.2%	Planetary mass companion (Chauvin et al. 2005b), very tentative planet candidate (15.5 AU, $\sim$5 $M_{\rm J}$) not detected at second epoch
SRX 1	06 22 30.9	−60 13 07.1	23.5	G1 V	1	0.07	AB Dor	6.5	5.2	5.4%	
HD 48189A	06 38 00.4	−61 32 00.2	21.7	G1/G2 V	1	0.07	AB Dor	6.2	4.7	1.8%	0.14″ binary
BD +23 1978	08 36 55.8	+23 14 48.0	41.6	K5 V	12	0.035	M01	8.7	6.5		
π_1UMa	08 39 11.7	+65 01 15.3	14.3	G1.5 V	12	0.21	Li from W03	5.6	4.3	0.1%	
LQ Hya	09 32 25.6	−11 11 04.7	18.3	K0 V	12	0.013	Li from W03	7.8	5.6	14%	
DX Leo	09 32 43.7	+26 59 18.7	17.7	K0 V	12	0.115	Her/Lyra	7	5.2	3.0%	Very tentative planet candidate (2.6 AU, $\sim$10 $M_{\rm J}$) not detected at second epoch
TWA 22	10 17 26.9	−53 54 28.0	22	M5	3	0.01		14	8.1		
HD 92945	10 43 28.3	−29 03 51.4	21.6	K1 V	12	0.07	AB Dor	7.8	5.8	8.0%	Very tentative planet candidate (10.4 AU, $\sim$6 $M_{\rm J}$) not detected at second epoch
GJ 417	11 12 32.4	+35 48 50.7	21.7	G0 V	13	0.115	Her/Lyra	6.4	5	0.0%	
TWA 4	11 22 05.3	−24 46 39.6	46.7	K4 V	2	0.01		9.1	5.8		0.78″ binary
TWA 25	12 15 30.8	−39 48 42.0	44.1	M0	3	0.01	TW Hydra	11	7.5	8.9%	
RX J1224.8−7503	12 24 47.3	−75 03 09.4	24.2	K2	14	0.016	Li from A95	11	7.8	9.3%	
RX J1231.9−7848	12 31 56.0	−78 48 36.0	50	M1	14	0.01	Li from A95	14	9.6		
EK Dra	14 39 00.2	+64 17 30.0	33.9	G0	15	0.07	AB Dor	7.6	6	0.4%	Binary (Metchev & Hillenbrand 2004)
HD 135363	15 07 56.3	+76 12 02.7	29.4	G5 V	12	0.0032	Li from W03	8.7	6.3	0.8%	0.26″ binary
KW Lup	15 45 47.6	−30 20 55.7	40.9	K2 V	16	0.002	Li from NB98	9.4	6.6	0.8%	
HD 155555AB	17 17 25.5	−66 57 04.0	30	G5 IV+K0 IV/V	8	0.012	β Pic	7.2	4.9	0.0%	
HD 155555C	17 17 27.7	−66 57 00.0	30	M4.5	8	0.012	β Pic	13	7.9	33%	
HD 166435	18 09 21.4	+29 57 06.2	25.2	G0	17	0.1	R'_{HK} from W2004	6.8	5.4	1.5%	
HD 172555A	18 45 26.9	−64 52 16.5	30	A5 IV/V	1	0.012	β Pic	4.8	4.3	2.6%	
CD −64 1208	18 45 37.0	−64 51 44.6	29.2	K7	8	0.012	β Pic	10	6.3	5.5%	0.18″ binary

TABLE 1—*Continued*

Target	R.A.[a] (J2000.0)	Decl. (J2000.0)	Distance (pc)[a]	SpT[b]	SpT Ref.	Age (Gyr)[c]	Age Ref.[c]	V[d]	H[e]	Detectability	Comments
Nearby Young Stars											
HD 181321	19 21 29.8	−34 59 00.5	20	G1/G2 V	16	0.16	Li from W03, R'_{HK} from G06	6.5	5	0.2%	Very tentative planet candidate (7 AU, ∼5 M_J) not detected at second epoch
HD 186704	19 45 57.3	+04 14 54.6	30.3	G0	17	0.2	R'_{HK} from W04	7	5.6	0.0%	
GJ 799B	20 41 51.1	−32 26 09.0	10.2	M4.5e	9	0.012	β Pic	13	. . .	20%	
GJ 799A	20 41 51.2	−32 26 06.6	10.2	M4.5e	9	0.012	β Pic	11	5.2	12%	
GJ 803	20 45 09.5	−31 20 27.1	9.94	M0 Ve	9	0.012	β Pic	8.8	4.8	23%	Very tentative planet candidate (3 AU, ∼2 M_J) not detected at second epoch
HIP 112312A	22 44 57.8	−33 15 01.0	23.6	M4e	3	0.012	β Pic	12	7.2	23%	Very tentative planet candidate (6.2 AU, ∼8 M_J) not detected at second epoch
HD 224228	23 56 10.7	−39 03 08.4	22.1	K3 V	16	0.07	AB Dor	8.2	6	6.8%	
More Distant Young Stars											
TWA 14	11 13 26.5	−45 23 43.0	66.7	M0	18	0.01	TW Hydra	13	8.7	3.5%	
RX J1243.6−7834	12 43 36.7	−78 34 07.8	150	M0	14	0.008	Li from A95	13	8.7		0.068″ binary
Stars with Known Radial Velocity Planets											
ϵ Eri	03 32 55.8	−09 27 29.7	3.22	K2 V	19	0.8	B06		1.9	0.0%	S. Kellner et al. (2007, in preparation), Janson et al. (2007)
HD 81040	09 23 47.1	+20 21 52.0	32.6	G0 V	12	2.5	Li from S06	7.7	6.3	0.0%	
HD 128311	14 36 00.6	+09 44 47.5	16.6	K0	12	0.63	R'_{HK} from G03	7.5	5.3	0.0%	
Nearby Solar Analogs											
HD 114613	13 12 03.2	−37 48 10.9	20.5	G3 V	16	4.2	Li from R93, R'_{HK} from G06	4.8	3.3	0.0%	
HD 201091	21 06 53.9	+38 44 57.9	3.48	K5 Ve	9	2.0[f]	R'_{HK} from G06	5.2	2.5	0.0%	
ϵ Ind A	22 03 21.7	−56 47 09.5	3.63	K4.5 V	9	1.3	L99	4.7	2.3	0.0%	Geissler et al. 2007
GJ 862	22 29 15.2	−30 01 06.4	15.4	K5 Ve	9	6.3[f]	R'_{HK} from G06	7.7	5.3	0.0%	

Note.—Units of right ascension are hours, minutes, and seconds, and units of declination are degrees, arcminutes, and arcseconds.

[a] Derived from the *Hipparcos* survey (Perryman et al. 1997).

[b] Spectral reference: (1) Houk & Cowley 1975; (2) Houk & Smith-Moore 1988; (3) Zuckerman & Song 2004 (4) Li & Hu 1998; (5) Christian & Mathioudakis 2002; (6) Leaton & Pagel 1960; (7) Favata et al. 1995; (8) Zuckerman et al. 2001a; (9) Gliesse & Jahreiss 1991; (10) Houk 1978; (11) Cutispoto et al. 1995; (12) Montes et al. 2001; (13) Bidelman 1951; (14) Alcala et al. 1995; (15) Gliesse & Jahreiss 1979; (16) Houk 1982; (17) Henry Draper Catalog; (18) Zuckerman et al. 2001b; (19) Cowley et al. 1967.

[c] Ages for stars with cluster memberships from Zuckerman & Song (2004), otherwise, ages are either lithium ages, calcium R'_{HK} ages, or an average of both. Acronyms for lithium and calcium age references: A95: Alcala et al. 1995, F97: Favata et al. 1997, LH98: Li & Hu 1998, NB98: Neuhäuser & Brandner 1998, R93: Randich et al. 1993, S06: Sozetti et al. 2006, and W03: Wichmann et al. 2003. Acronyms for other age references: B06: Benedict et al. 2006, G03: Gray et al. 2003, G06: Gray et al. 2006, L05: Lowrance et al. 2005, L99: Lachaume et al. 1999, M01: Montes et al. 2001, and W04: Wright et al. 2004. The expression "mg" stands for "moving group."

[d] From the CDS Simbad service.

[e] From the 2MASS Survey (Cutri et al. 2003).

[f] In general, we have only determined Ca R'_{HK} ages for stars with spectral types K1 or earlier, but in the case of these two K5 stars, we have only the R'_{HK} measurement on which to rely for age determination. The calibration of the Mount. Wilson *S*-index to R'_{HK} for K5 stars ($B - V \sim 1.1$ mag) has not been well-defined (Noyes et al. 1984; specifically the photospheric subtraction), and hence applying a R'_{HK} vs. age relation for K5 stars is unlikely to yield useful ages. Although we adopt specific values for the ages of these stars, it would be more accurate to state simply that these stars have ages > 1 Gyr. As a result, almost all simulated planets are too faint to detect around these stars, so the precise error in the age does not significantly affect our final results.

TABLE 2
VLT SDI Observation Log

Object	Date	DIT (s)	NDIT (s)	Total Exp. (minutes)
HIP 1481	2004 Nov 15	14	6	56
	2005 Nov 24	16	5	26.7
	2005 Nov 25	16	5	26.7
	2005 Nov 27	16	5	26.7
ERX 6	2004 Nov 14	22	4	29.3
	2004 Nov 16	22	4	58.7
ERX 8	2004 Nov 17	22	4	58.7
HIP 9141	2004 Sep 27	14	6	56
BD +05 378	2005 Feb 01	32	3	25.6
HD 17925	2003 Aug 14	7.5	16	40
	2003 Aug 16	4	30	40
	2003 Aug 17	4	30	20
	2004 Feb 02	1	120	20
	2004 Nov 16	4.1	17	46.5
	2004 Nov 17	4.1	17	46.5
LH 98 062	2004 Feb 03	14	9	21
ϵ Eri	2004 Sep 19	0.6	160	64
V834 Tau	2005 Jan 25	10	9	24
	2005 Feb 01	10	9	24
GJ 182	2004 Feb 02	7	17	39.7
	2005 Nov 22	20	4	26.7
	2005 Nov 24	20	4	26.7
	2005 Nov 27	20	4	26.7
HIP 23309	2005 Jan 30	24	4	25.6
	2005 Jan 31	24	4	51.2
AB Dor	2004 Feb 02	5	24	20
	2004 Sep 28	12	7	28
	2004 Nov 16	10.4	8	27.7
GJ 207.1	2005 Jan 27	32	3	25.6
UY Pic	2004 Nov 16	14	6	28
	2004 Nov 17	14	6	56
AO Men	2004 Feb 03	14	9	21
	2005 Nov 15	30	1	17.5
	2005 Nov 24	30	1	10
AB Pic	2004 Nov 14	20	4	26.7
	2004 Nov 15	20	4	26.7
	2005 Nov 22	20	4	13.3
	2005 Nov 25	20	4	53.3
SRX 1	2004 Nov 18	12	7	28
	2004 Nov 19	12	7	28
HD 48189A	2004 Nov 17	6.5	11	23.8
	2004 Nov 18	6.5	11	23.8
BD +23 1978	2005 Jan 27	24	4	25.6
	2005 Jan 28	24	4	25.6
LQ Hya	2004 Feb 02	5	24	40
	2004 Dec 08	14	6	28
	2004 Dec 14	14	6	28
DX Leo	2004 Feb 05	3	38	19
	2005 Dec 04	14	6	28
	2005 Dec 19	14	6	28
TWA 22	2005 Jan 25	32	1	48.5
HD 92945	2004 Feb 05	5	24	60
TWA 14	2005 Jan 28	32	3	25.6
	2005 Jan 29	32	3	25.6
TWA 4	2004 Feb 02	7	17	9.92
TWA25	2005 Jan 28	32	3	25.6
RX J1224.8−7503	2004 Feb 02	40	3	20
	2005 Jan 16	30	3	60
	2005 Jan 27	30	3	120
RX J1231.9−7848	2004 Feb 05	20	6	20
RX J1243.6−7834	2004 Feb 02	5	24	40
HD 114613	2004 Feb 02	1	120	40
KW Lup	2004 Sep 15	22	4	14.7
	2004 Sep 16	24	4	22.7
	2004 Sep 17	24	4	24
HD 155555AB	2003 Aug 14	7.5	16	10
	2003 Aug 15	7.5	16	20
	2003 Aug 16	7.5	16	10
	2003 Aug 17	7.5	16	10
	2004 Sep 16	10	9	30
	2004 Sep 18	14	6	28
HD 155555C	2003 Aug 14	30	4	40
	2003 Aug 16	30	4	40
HD 172555A	2003 Aug 17	5	24	20
	2004 Sep 17	5	15	25
	2004 Sep 18	5	15	6.25
	2004 Sep 19	5	15	18.8
CD −64 1208	2003 Aug 17	20	6	40
	2004 Sep 16	15	6	30
HD 181321	2003 Aug 15	7.5	16	40
	2004 Sep 18	11	8	29.3
GJ 799B	2003 Aug 16	20	6	40
	2003 Aug 17	20	6	30
	2004 Sep 19	15	6	30
GJ 799A	2003 Aug 16	20	6	40
	2004 Sep 16	10	9	30
	2004 Sep 19	15	6	30
GJ 803	2003 Aug 14	7.5	18	56.2
	2003 Aug 15	10	12	40
	2003 Aug 17	7.5	16	40
	2004 Sep 17	6	15	30
	2004 Sep 18	10	9	30
ϵ Ind A	2004 Sep 18	0.5	192	48
GJ 862	2003 Aug 15	10	12	40
	2003 Aug 16	10	12	40
	2004 Sep 19	13	7	48.2
HIP 112312A	2004 Sep 19	25	4	66.7
HD 224228	2003 Aug 16	10	12	40
	2003 Aug 17	20	6	40
	2004 Oct 08	14	6	28
	2004 Oct 20	21	4	28

(for instance, the Li λ6707, the Ca H and K lines, and Hα emission), as well as from X-ray emission, variability, and rotational speed.

As moving group ages are generally more robust than measurements for individual stars, we expect the ages of stars in these associations, on average, to have greater accuracy. Our survey covers stars in the β Pic, TW Hya, AB Dor, IC 2391, and Tucanae/Horologium moving groups.

We select target stars based on two overlapping criteria: (1) stars within 25 pc and younger than 250 Myr and (2) stars within 50 pc and younger than 40 Myr (see Fig. 4). Our original list has been modified according to the amount of allocated time at the telescope, the unavailability of GTO targets, as well as severe weather constraints for the MMT portion of our survey. At the VLT, our observing runs spanned the months of August through February over 2004 and 2005. Thus, due to the spacing of observing runs, in the south, the survey is close to complete from ∼17–13 hr R.A. At the MMT, we had two observing runs, one in 2005 May and one in 2006 February. Thus, in the north, the survey is complete for the R.A. range 11–21 hr.

Survey objects are presented in Table 1. A detailed table of observations is presented in Tables 2 and 3. Survey objects are plotted as a function of distance and age in Figure 4. Our "median" survey object is a K star with an age of 30 Myr and at a distance of 25 pc.

TABLE 3
MMT SDI Observation Log

Object	Date	DIT (s)	NDIT (s)	Total Exp. (minutes)
V577 PerA	2006 Feb 12	20	7	37.3
	2006 Feb 13	21.5	7	40.1
HIP 30030	2006 Feb 12	30	5	30
π_1 UMa	2006 Feb 13	5.8	13	40.2
HD 81040	2006 Feb 12	11.7	13	40.3
LQ Hya	2006 Feb 12	8	19	40.5
DX Leo	2005 May 01	10	13	34.7
GJ 417	2005 Apr 30	7	17	31.7
HD 128311	2006 Feb 12	4	19	60.8
EK Dra	2005 May 01	20	7	37.3
HD 135363	2005 May 01	30	5	40
HD 166435	2005 Apr 30	7	17	31.7
	2005 May 01	7	17	31.7
HD 186704	2005 May 01	10	13	17.3
HD 201091	2005 Apr 30	20	7	37.33

3.2. *The Performance of the SDI Filters as Spectral Indices*

It is important to carefully consider the expected strength of the 1.62 μm methane absorption break used by the SDI device. The stronger the break strength, the more companion light is preserved after SDI filter subtraction. For a candidate object with a weak break strength, SDI subtraction may effectively attenuate the candidate object itself, rendering it undetectable (although, at separations $> 0.15''$, a bright object may still be detectable due to the characteristic dark-light radial pattern produced by any real object after pipelining; see § 2.2.)

To determine the methane-break strength expected for a candidate object (and thus, the expected performance of SDI for that candidate), we define an SDI methane spectral index calculated from our SDI F1(1.575 μm) and F3(1.625 μm) filter images (similar to the methane spectral index defined by Geballe et al. [2002]).

$$\text{index}\left(\frac{\text{F1}}{\text{F3}}\right) = \frac{\int_{\lambda_1=1.5625\ \mu\text{m}}^{\lambda_2=1.5875\ \mu\text{m}} S_\lambda \text{F1}(\lambda)\, d\lambda}{\int_{\lambda_3=1.6375\ \mu\text{m}}^{\lambda_4=1.6125\ \mu\text{m}} S_\lambda \text{F3}(\lambda)\, d\lambda}. \qquad (4)$$

Each SDI filter was manufactured by Barr Associates to have a precise bandwidth of 0.025 μm, so the wavelength intervals ($\lambda_2 - \lambda_1 = \Delta\lambda = \lambda_4 - \lambda_3$) in the numerator and denominator have the same length for the SDI methane index.

We calculated SDI spectral indices for the four brown dwarfs which have been observed with SDI—the T6 Gl 229B (Nakajima et al. 1995), the T5.5 SCR 1845B (Biller et al. 2006b), and ϵ Ind Ba-Bb (T6+T1) (McCaughrean et al. 2004). Since we only possess SDI data on a limited number of T dwarfs, we calculated the same SDI spectral indices from spectra of 56 L dwarfs and 35 T dwarfs (Knapp et al. 2004) in order to evaluate the performance of the SDI for a wide range of L and T dwarf objects. Spectra for these objects were obtained from Sandy Leggett's L and T dwarf archive.[10] In order to make an accurate comparison, SDI filter transmission curves were convolved into these calculations (see Fig. 1). Since we have full spectral data for these objects, we also calculated the 1.62 μm methane spectral indices defined by Geballe et al. (2002) which were found to be similar to our SDI methane spectral indices. SDI methane spectral indices are plotted for both the M9 and T6 components of SCR 1845, the T dwarfs Gl 229B, ϵ Ind Ba, ϵ Ind Bb, and 94 other L and T dwarfs in Figure 5. Geballe et al. (2002) note that Gl 229B has an anomalously high methane index for its spectral type and assign a large uncertainty to Gl 229B's spectral type, T6 ± 1, which is also reflected in its anomalously large SDI spectral index compared to other T6 dwarfs. From this analysis, we conclude that the SDI device can effectively detect objects with spectral type later than T3. Since T dwarfs with spectral type earlier than T3 are relatively uncommon compared to later T dwarfs, the SDI device can effectively detect the full range of extrasolar giant planet/brown dwarf spectral types of interest. According to the models of Burrows et al. (2003) and Marley et al. (2006), planets > 10 Myr old should possess $T_{\text{eff}} < 800$ K and have spectral type of T8 or greater.

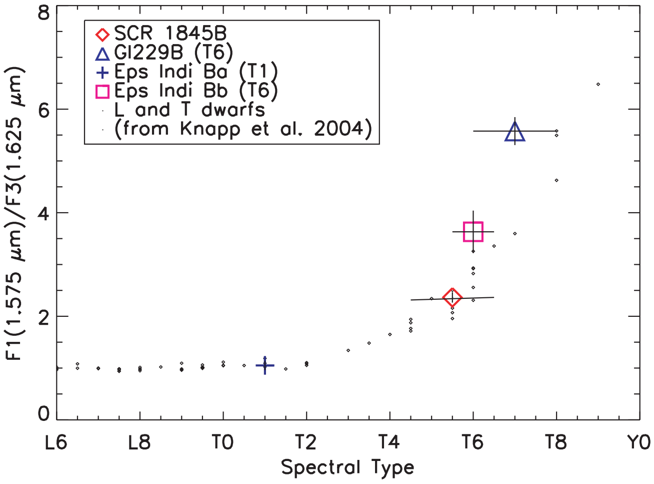

Fig. 5.—SDI methane spectral indices for the T dwarfs SCR 1845B, Gl 229B, ϵ Ind Ba, and ϵ Ind Bb (from Biller et al. 2006b). As a comparison, SDI methane spectral indices calculated from spectra for 94 L and T dwarfs (spectra from Knapp et al. 2004) are overplotted. SCR 1845B, Gl 229B, and ϵ Ind Bb show strong methane indices, whereas ϵ Ind Bb (T1) is relatively constant in flux across the SDI filters and has a much lower methane index. Geballe et al. (2002) note that Gl 229B has an anomalously high methane index for its spectral type. While Geballe et al. (2002) find an overall spectral type of T6 ± 1 for Gl 229B, they assign Gl 229B a spectral type of T7 based on the methane index (which we adopt here).

3.3. *Contrast Limits and Minimum Detectable Planet Separation*

To determine the range of possible star-planet contrasts achieved in our survey, we generated noise curves as a function of radius for every survey star. We tested three different methods of generating noise curves: (1) translating a 6×6 pixel ($0.1'' \times 0.1''$) box along a particular radial trajectory away from the center of the star image (typical PSF FWHM was 3–5 pixels) and then calculating the standard deviation in the box at each point along this trajectory, (2) averaging noise curves generated along four such trajectories, and (3) calculating the standard deviation within annular regions 6 pixels in width centered on the primary PSF (spider diffraction spikes were not masked out in this case because they are already well removed by the spectral difference). Noise curves generated in these three manners are presented for a set of six typical program stars (AB Dor, DX Leo, GJ 182, AB Pic, GJ 799A, and GJ 799B) in Figure 6. In general, all three methods produce remarkably similar noise curves and are equally suitable for characterizing the noise properties of an observation. However, we choose to use the single-trajectory method because it best simulates the particular S/N issues encountered when searching for

---

[10] See http://www.jach.hawaii.edu/~skl/LTdata.html.

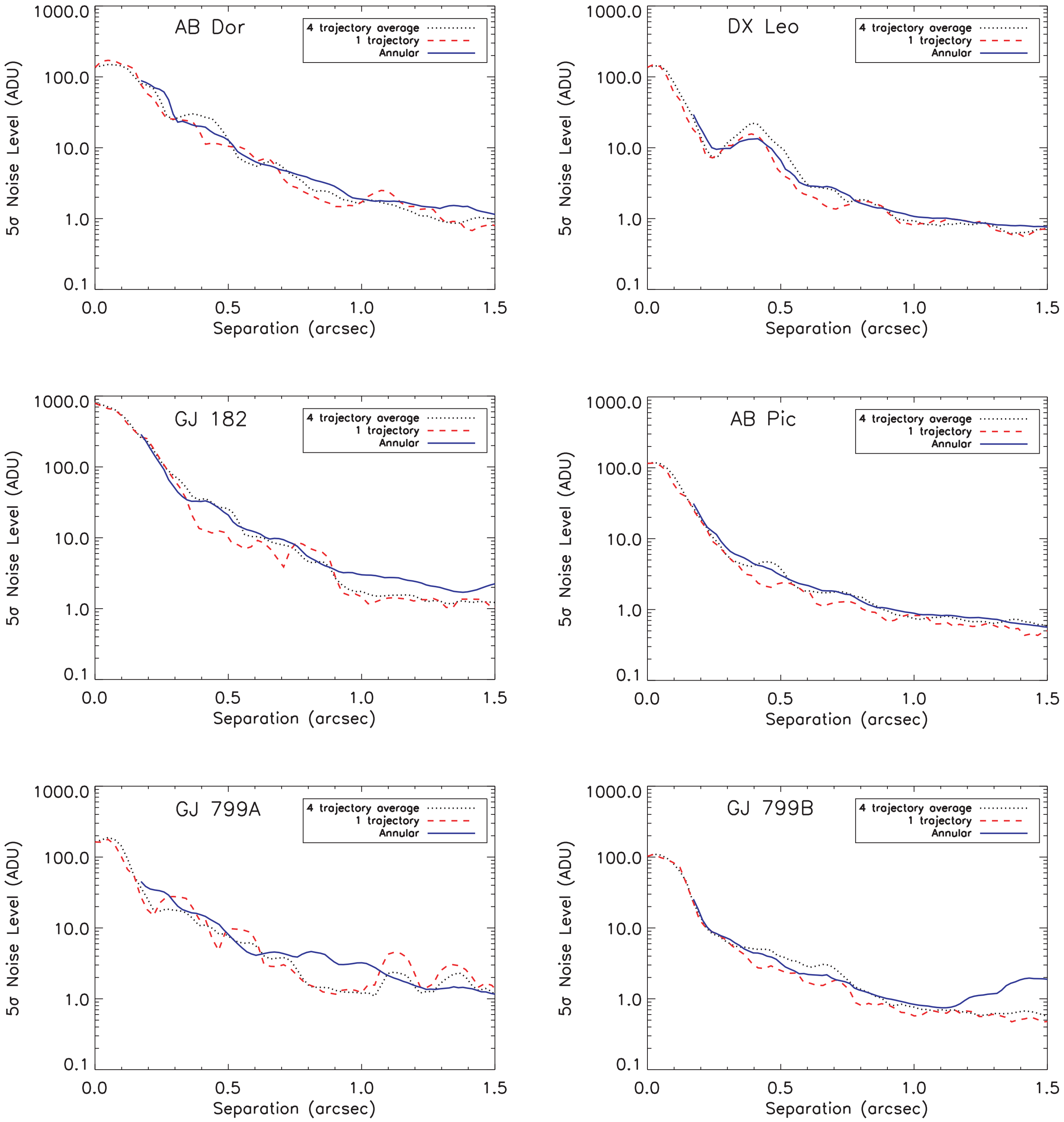

Fig. 6.—Comparison of noise curves generated in three different manners for a set of six typical program stars (*upper left*, AB Dor; *upper right*, DX Leo; *middle left*, GJ 182; *middle right*, AB Pic; *lower left*, GJ 799A; *lower right*: GJ 799B). Noise curves were generated by (1) translating a 6×6 pixel ($0.1'' \times 0.1''$) box along a particular radial trajectory away from the center of the star image (typical PSF FWHM was 3–5 pixels) and then calculating the standard deviation in the box at each point along this trajectory, (2) averaging noise curves generated along four such trajectories, and (3) calculating the standard deviation within annular regions 6 pixels in width centered on the primary PSF (spider diffraction spikes were not masked out in this case because they are already well removed by the spectral difference). In general, all three methods produce remarkably similar noise curves and are equally suitable for characterizing the noise properties of an observation. Since it preserves pixel-to-pixel contrast variations due to speckle noise, the single-trajectory method better simulates the S/N issues encountered in searching for faint companions.

faint companions among superspeckles of similar intensity and FWHM (since it preserves pixel-to-pixel noise variations due to superspeckles). The annular method averages out speckle noise properties azimuthally. This produces somewhat unrealistic results in the case of a faint companion search where one is concerned only with the speckle structure within the local area of a candidate faint companion; speckle structure on the other side of the image is unimportant. In addition, we have tried to choose a very "typical" trajectory per star; ideally, trajectory-to-trajectory variations will average out across the entire survey.

Noise curves for each program star were calculated along a trajectory 45° from the image *x*-axis in the first quadrant. This was selected as one of many possible representative trajectories which was unaffected by instrumental effects such as spider

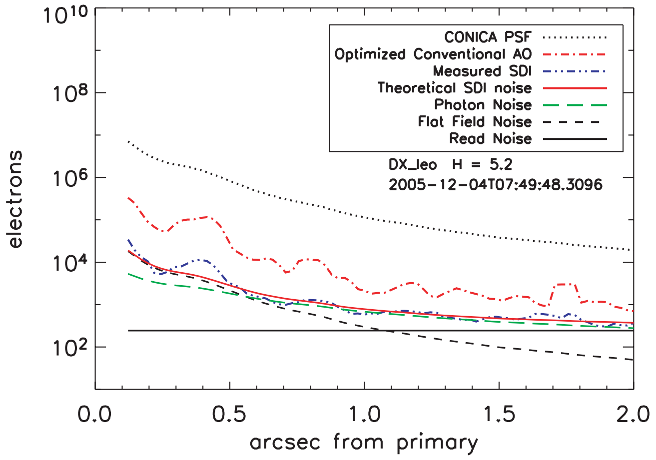

FIG. 7.—Sensitivity curve for DX Leo (18 pc, K0 V, 115 Myr, $V = 7.05$, $H = 5.242$). This is 28 minutes of VLT SDI data. The CONICA PSF curve is the median combination of all the F1(1.575 μm) filter images for this data set (with a gain correction applied which accounted for the number of exposures, dithers, and roll angles). The "optimized conventional AO" curve was generated by averaging images from all three filters at each roll angle, unsharp masking to remove low spatial frequencies, and then subtracting the combinations at different roll angles from each other. The "measured SDI" data curve is the full reduced and differenced SDI data for this object [F1(1.575 μm) − F3a(1.625 μm) for two roll angles]. The "theoretical SDI noise" curve is calculated from photon noise (*dashed green curve*), flat-field noise (*dashed black curve*), and read noise (*solid black line*) added in quadrature. Within 0.5″, the SDI data are "flat-field"-noise limited. (In reality, we are limited by superspeckle residuals within this radius. Our flat fields are accurate to the ~1% level, but the speckle residuals <0.5″ vary more than this and thus dominate the SDI noise.) From 0.5″ onward, the SDI data are photon-noise limited, asymptotically approaching the read-noise limit at separations > 2″. For a complete set of sensitivity curves, see http://exoplanet.as.arizona.edu/~lclose/SDI.html.

arms, vibrations along azimuth or altitude mounts, etc. At each point along this trajectory, the standard deviation was calculated (except for the PSF noise curve, for which the mean was calculated).

A fully labeled, example noise curve for the star DX Leo is presented in Figure 7. Noise curves were generated for a number of cases for each object. First, a noise curve was generated for the full reduced and differenced SDI data (labeled measured SDI data) [F1(1.575 μm) − F3a(1.625 μm) for two roll angles]. A PSF noise curve was generated from a median combination of all the F1(1.575 μm) filter images for each data set, weighted according to the number of exposures, dithers, and roll angles in the data set. To recreate the equivalent observation without using the SDI technique (and thus characterize the performance of SDI compared to conventional AO techniques), an "optimized conventional AO" curve was generated by combining images from all three filters at each roll angle:

$$\begin{aligned}\text{Broadband} = {} & \text{F1}(1.575\ \mu\text{m}) \\ & + \text{F2}(1.6\ \mu\text{m}) + \text{F3}(1.625\ \mu\text{m}) \qquad (5)\end{aligned}$$

then unsharp masking to remove low spatial frequencies, and subtracting the "broadband" combinations at different roll angles from each other.

To characterize the noise level in each observation, we calculated an SDI noise curve, which is a combination of photon noise, flat-field noise, and read noise. Per exposure

$$\sigma_{\rm SDI} = \sqrt{\sigma_{\rm ph}^2 + \sigma_{\rm flat}^2 + \sigma_{\rm read}^2}. \qquad (6)$$

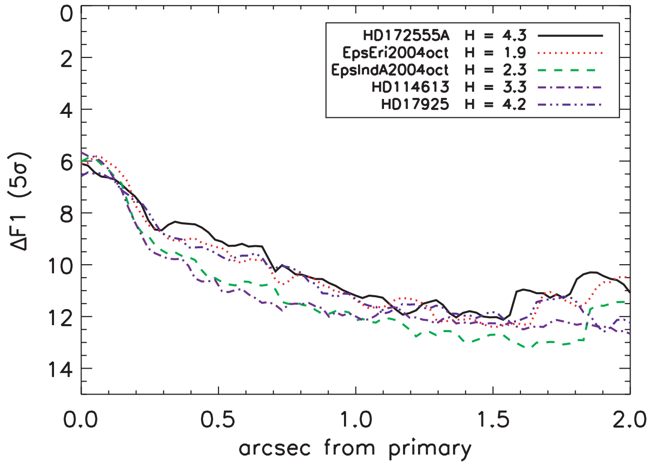

FIG. 8.—The 5 σ Contrasts for VLT SDI survey objects with $H < 4.5$ in the F1(1.575 μm) filter. These contrast curves were generated by translating a 6 × 6 pixel (0.1″ × 0.1″) box along a particular radial trajectory away from the center of the star and then calculating the standard deviation within that box as a function of radius. Curves were generated from the full reduced and differenced SDI data for each object [F1(1.575 μm) − F3a(1.625 μm) for two roll angles].

Photon noise was calculated as

$$\sigma_{\rm ph} = \sqrt{n_e}, \qquad (7)$$

where n_e is the number of electrons. Readout noise for the CONICA detector at the VLT in Fowler sampling mode is 1.3 ADU (analog-to-digital unit). The gain for the latest CONICA detector in the Fowler sampling mode is 12.1 e ADU^{-1} so $\sigma_{\rm read} = 15.73\ e$.

NACO and ARIES flat fields were found to be accurate to about 1%, so flat-field noise was estimated as

$$\sigma_{\rm flat} = \epsilon n_e, \qquad (8)$$

where $\epsilon = 0.01$. The total noise for a full observation (four to five dithers and two to four roll angles) was then calculated by weighting the SDI noise per exposure by the number of exposures (NDIT × number of dithers × number of roll angles):

$$\begin{aligned}\sigma_{\rm SDIfullobs} = \sigma_{\rm SDI}(& \text{NDIT} \\ & \times \text{number of dithers} \\ & \times \text{number of roll angles})^{1/2}. \qquad (9)\end{aligned}$$

The PSF curve for a full observation was similarly weighted:

$$\begin{aligned}\text{PSF} = \text{medianPSF} & \times \text{NDIT} \\ & \times \text{number of dithers} \\ & \times \text{number of roll angles}. \qquad (10)\end{aligned}$$

For the sample curve shown in Figure 7, the SDI data are "flat-field" limited within 0.5″ of the star. From 0.5″ onward, the SDI data are photon-noise limited, approaching the read-noise limit at separations > 2″.

We converted our noise in electrons to attainable contrasts in magnitudes in the F1(1.625 μm) filter; contrast plots in Δmag are presented for all nonbinary survey objects in Figures 8–14 according to the H magnitude of the primary for the VLT and

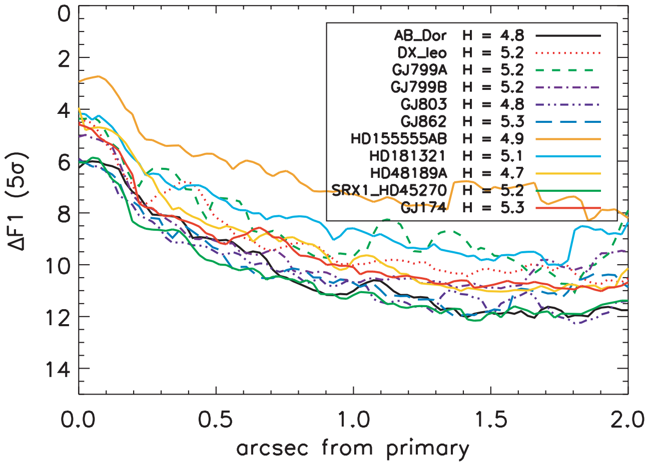

FIG. 9.—Same as Fig. 8, but for VLT SDI survey objects with $5.5 > H > 4.5$.

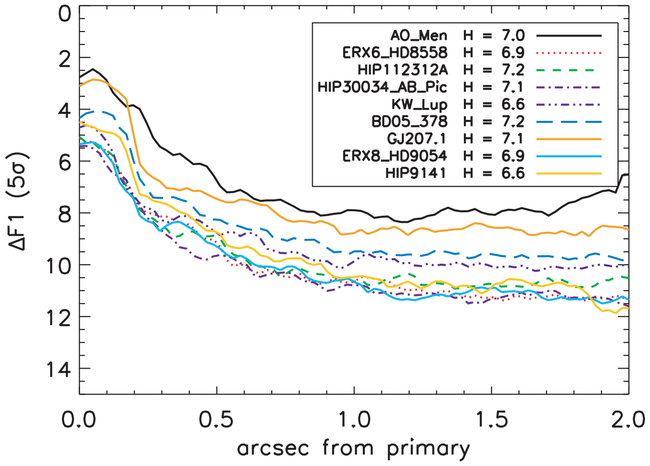

FIG. 11.—Same as Fig. 8, but for VLT SDI survey objects with $7.5 > H > 6.5$.

according to observing run for the MMT. For every observation which possesses an unsaturated acquisition image (typically 10×0.1 s images taken over $\sim$30 s), the stellar peak in the unsaturated acquisition image was used to scale the saturated stellar peak in the saturated data images and thus attain accurate contrasts in magnitudes. For observations lacking an unsaturated acquisition image, contrast curves for other stars which had similar peaks, read-noise values, and shapes to the contrast curve in question were selected from the library of contrast plots in electron units. The peaks used for these matching contrast curves were then used to scale the observation missing an acquisition image. A peak of 2.2×10^5 was adopted for ϵ Eri (S. Kellner et al. 2007, in preparation; Janson et al. 2007) and ϵ Ind A (Geissler et al. 2007). We present contrast curves for 48 stars in this paper; the remaining six survey stars were either very close binaries, making it difficult to generate a contrast curve, or had particularly low quality data sets.

For the VLT data, attainable contrast depends on the primary star H magnitude, as well as the seeing FWHM and Strehl ratio during the observation. For the brightest stars in the survey ($H < 4.5$), we attain 5 σ contrasts of ΔF1 $\sim$ 12 mag at separations of $>1''$ from the star. For the faintest survey stars, we only attain 5 σ contrasts of ΔF1 $\sim$ 10 mag $>1''$ from the star. However, considerable spread in attained contrast is observed in each H magnitude bin, most likely due to variations in observing conditions (seeing, Strehl ratio, etc.) across multiple observations. To quantify the effect of seeing on attainable contrast, in Figure 15 we plot the seeing FWHM (averaged over the observation; the error bars on seeing are the seeing variations as measured by the standard deviation of the seeing over each observation) versus attained 5 σ contrast at $0.5''$ for 10 of the stars presented in Figure 9 with H magnitudes between 4.5 and 5.5. For this sample of stars with similar H magnitudes, achievable contrast is roughly inversely proportional to the seeing FWHM. A fair amount of scatter is apparent in this plot and is due in part to seeing variations over the course of each observations. Seeing FWHM can vary considerably over the 20–40 minute timescale of a typical SDI observation, affecting the AO system performance and thus the achievable contrast.

However, higher attained contrast does not necessarily translate across the board to a lower minimum detectable planet mass. Although one might be able to attain a very high contrast (5 σ contrast of >11 mag at $1''$ limited by photon noise) for a bright young A star, one would have more luck searching for low-luminosity planets around an intrinsically faint young M star (5 σ contrast of $\sim$9 mag at $1''$ limited by read noise), since the inherent contrast difference expected between star and planet is considerably smaller. We obtained contrasts of $\Delta H > 10$ mag (5 σ) at $0.5''$ for 45% of target objects at the VLT and contrasts of $\Delta H > 9$ mag (5 σ) at $0.5''$ for 80% of our targets. This is more a

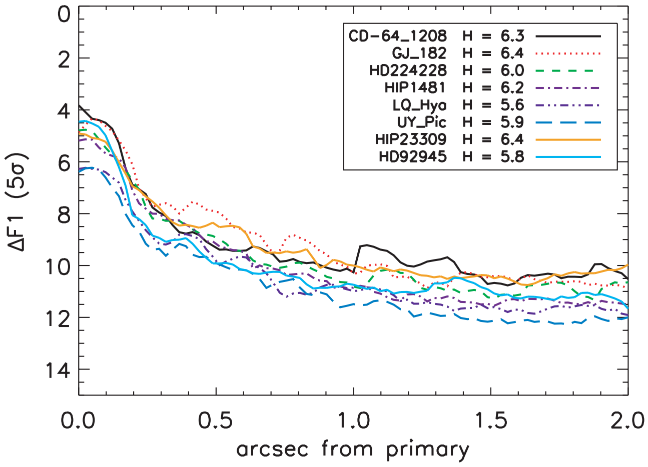

FIG. 10.—Same as Fig. 8, but for VLT SDI survey objects with $6.5 > H > 5.5$.

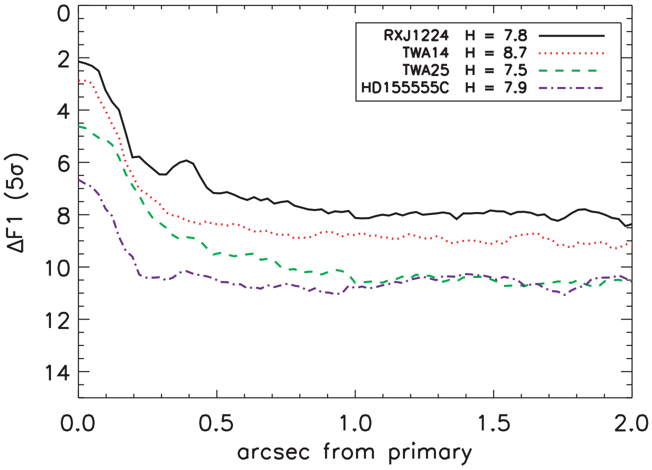

FIG. 12.—Same as Fig. 8, but for VLT SDI survey objects with $H > 7.5$.

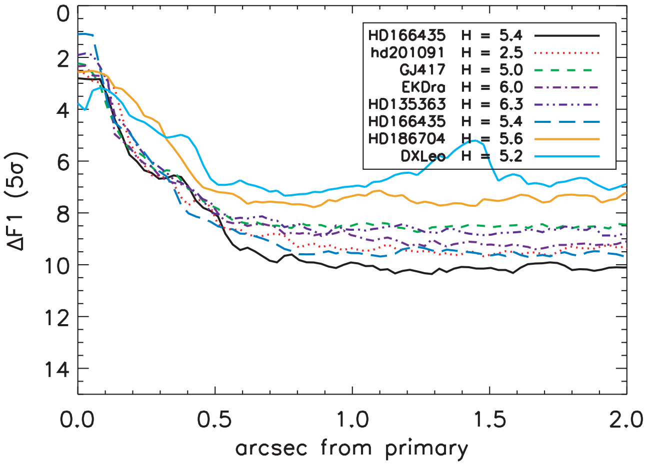

Fig. 13.—Same as Fig. 8, but for the MMT SDI survey objects observed in 2005 May.

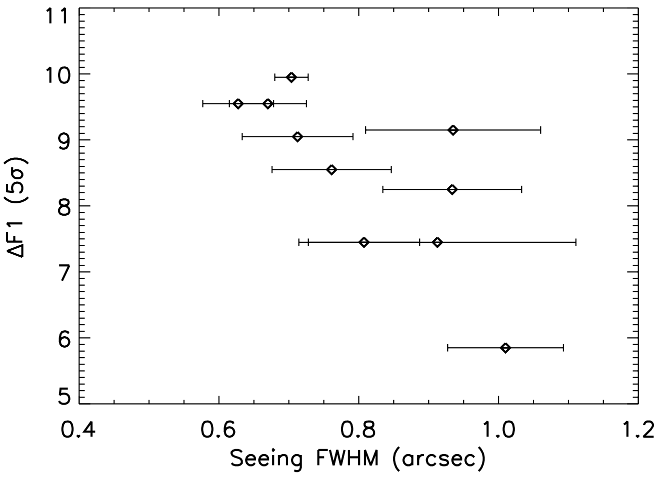

Fig. 15.—Seeing FWHM (averaged over each observation) vs. attained 5 σ contrast at 0.5″ separation from the primary star for 10 of the stars presented in Fig. 9 with H magnitudes between 4.5 and 5.5. The error bars on seeing are the seeing variation (as measured by the standard deviation of the seeing) over each observation. For this sample of stars with roughly the same H magnitude, the achievable contrast varies roughly inversely with the average seeing FWHM. Scatter in this plot is in part due to the fact that the seeing FWHM can change considerably over a 20–40 minute long observation.

statement on the spectral types in our sample than a performance-related issue.

In general, the MMT SDI device performed at a slightly lower level than the VLT SDI device, attaining 5 σ contrasts 0.5–1 mag less than those achieved at the VLT for similar separations and primary-star H magnitudes. The lesser performance of the MMT system can be attributed to two factors. First, the diameter of the MMT is 6.5 m versus the VLT which has an 8.2 m diameter, resulting in a considerable decrease in sensitivity. In addition, the seeing sampled by the MMT AO system was not as stable as for the NACO AO system: Strehl ratios often changed dramatically over an observation, limiting the attainable contrast. However, the MMT SDI results still probe a higher contrast regime at separations $< 1''$ than is possible with standard AO techniques.

In order to determine what objects realistically can be detected for our survey stars, we must convert between our instrumental F1(1.625 μm) filter magnitudes and H-band magnitudes and then compare the H magnitudes to those expected from models of young planets (such as Burrows et al. 2003). To accomplish this, the spectra of both the primary and secondary components of each target must be taken into account. To convert from our F1 filter magnitudes into calibrated H-band magnitudes, we must calculate the H-band magnitude offsets for both the primary star and a potential methane companion (Offset$_A$ and Offset$_B$, respectively):

$$\begin{aligned}\Delta H &= H_A - H_B\\ &= (\mathrm{Offset}_B + \mathrm{F1}_B) - (\mathrm{Offset}_A + \mathrm{F1}_A)\\ &= (\mathrm{Offset_B} - \mathrm{Offset}_A) + \Delta\mathrm{F1} \qquad (11)\end{aligned}$$

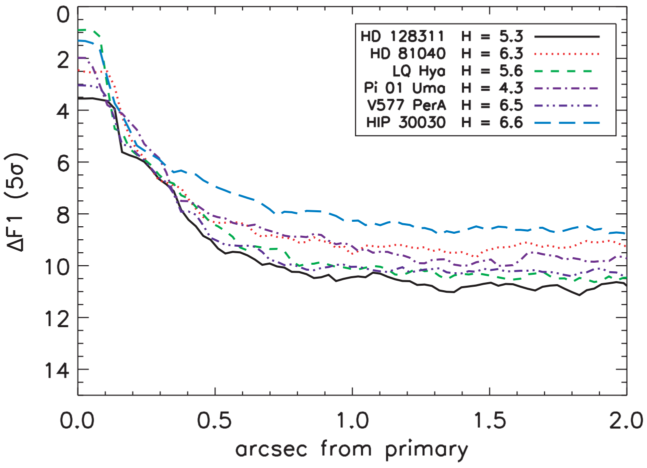

Fig. 14.—Same as Fig. 8, but for MMT SDI survey objects observed in 2006 February.

For primary stars with spectral types F–K, we assume that the star has very little chromatic variation within the middle of the H band, so Offset$_A$ is zero (see Fig. 1). For lower mass M stars, which are very red, the magnitude offset is not negligible. To take an extreme example, a very low mass M8 primary will have a magnitude offset of Offset$_A = -0.12 \pm 0.08$ mag (calculated using the spectrum of the M8 star VB 10, an H transmission curve, and our F1 filter transmission curve). The latest stars in our survey have spectral type M0–M5, so Offset$_A$ will be <0.1 mag for these cases.

Any T3 or later companion to one of our survey stars will be blue compared to the primary and will appear “brighter” in the F1 filter than in the H band (in other words, it will have a higher “flux” in the F1 filter [number of photons per unit bandwidth]; see Fig. 1), so Offset$_B$ will definitely be nonnegligible. We calculated Offset$_B$ for 18 objects with spectral types of T4.5–T8 (spectra from Knapp et al. 2004) and then averaged together by spectral type to derive an average offset for each spectral type. For a T5 companion, $\mathrm{Offset_{T5}} = 0.5 \pm 0.05$ mag; for a T6 companion, $\mathrm{Offset_{T6}} = 0.6 \pm 0.07$ mag; and for a T8 companion, $\mathrm{Offset_{T8}} = 0.87 \pm 0.04$ mag. While we do not convert our full ΔF1 contrast plots to ΔH contrast plots, for every survey star we calculate limiting ΔH contrasts (5 σ values), at 0.5″ and 1.0″, equivalent separation in AU, apparent H magnitude, and absolute H magnitude for a T8 spectral-type companion (since extrasolar planets are expected to have spectral type $\gtrsim$ T8; Burrows et al. 2003). These results are presented in Tables 4 and 5. However, it is difficult to translate our absolute H magnitudes into model planet masses since we have assumed a T8 spectral type in

TABLE 4

Limiting H Magnitude (5 σ) at 0.5″

Object	ΔF1	Separation (AU)	ΔH (T8 SpT)	m_H	M_H
ϵ Eri	9.4 ± 0.12	1.61	10.3	12.2	14.7
ϵ Ind A	10.6 ± 0.12	1.81	11.5	13.8	16
HD 201091	8.08 ± 0.52	1.74	8.95	11.5	13.8
HD 114613	6.13 ± 0.26	10.2	7	10.3	8.74
HD 17925	9.69 ± 0.14	5.19	10.6	14.8	14.7
HD172555A	9.14 ± 0.12	15	10	14.3	11.9
π_1 UMa	8.04 ± 0.15	7.14	8.91	13.2	12.4
HD 48189A	8.54 ± 0.052	10.8	9.41	14.2	12.5
GJ 803	9.54 ± 0.091	4.97	10.4	15.2	15.2
AB Dor	9.04 ± 0.019	7.47	9.91	14.8	13.9
HD 155555AB	5.87 ± 0.14	15	6.74	11.6	9.21
GJ 417	7.79 ± 0.23	10.9	8.66	13.7	12
HD 181321	7.42 ± 0.13	10	8.29	13.3	11.8
SRX 1	9.95 ± 0.079	11.7	10.8	16	14.1
GJ 799A	7.48 ± 0.082	5.11	8.35	13.6	13.6
DX Leo	8.24 ± 0.19	8.87	9.11	14.4	13.2
GJ 862	9.51 ± 0.25	7.72	10.4	15.7	14.8
V834 Tau	9.08 ± 0.18	6.74	9.95	15.3	14.6
HD 166435	8.42 ± 0.17	12.6	9.29	14.7	12.7
LQ Hya	9.82 ± 0.16	9.17	10.7	16.3	15
HD 186704	7.13 ± 0.091	15.1	8	13.6	11.2
HD 92945	9.91 ± 0.0099	10.8	10.8	16.6	14.9
UY Pic	9.96 ± 0.11	11.9	10.8	16.7	14.8
HD 224228	9 ± 0.15	11	9.87	15.9	14.2
EK Dra	7.85 ± 0.39	17	8.72	14.7	12
HIP 1481	9.22 ± 0.13	20.5	10.1	16.3	13.2
CD −64 1208	9.33 ± 0.087	14.6	10.2	16.5	14.2
HD 135363	7.9 ± 0.27	14.7	8.77	15.1	12.8
HIP 23309	8.45 ± 0.092	13.1	9.32	15.7	13.6
GJ 182	8.01 ± 0.16	13.3	8.88	15.3	13.2
V577 PerA	8.9 ± 0.33	16.9	9.77	16.2	13.6
HIP 9141	8.92 ± 0.29	21.2	9.79	16.3	13.2
HIP 30030	6.91 ± 0.17	26.2	7.78	14.4	10.8
KW Lup	8.76 ± 0.091	20.5	9.63	16.3	13.2
ERX 8	9.4 ± 0.2	18.6	10.3	17.2	14.4
ERX 6	9.38 ± 0.4	24.6	10.2	17.1	13.6
AO Men	6.91 ± 0.33	19.2	7.78	14.8	11.9
AB Pic	9.65 ± 0.027	22.8	10.5	17.6	14.3
GJ 207.1	7.5 ± 0.094	8.41	8.37	15.5	14.4
HIP 112312A	9.09 ± 0.27	11.8	9.96	17.1	15.2
BD +05 378	8.31 ± 0.088	20.3	9.18	16.4	13.4
TWA 25	9.5 ± 0.035	22	10.4	17.9	14.7
RX J1224.8−7503	7.16 ± 0.024	12.1	8.03	15.9	14
HD 155555C	10.5 ± 0.085	15	11.4	19.3	16.9
TWA 14	8.38 ± 0.03	33.3	9.25	18	13.9

our conversion between ΔF1 and ΔH contrasts, but a companion which actually has the limiting absolute H magnitude we find (combined with the known age and distance of the system) may have a very different spectral type.

Since we cannot translate our H magnitudes directly into planetary mass companions, we followed the analysis of Masciadri et al. (2005), translated theoretical planet models (Burrows et al. 2003; Baraffe et al. 2003) into H magnitudes, and then determined the minimum separation at which such a companion could be detected (at the 5 σ level) in our survey. The minimum separation at which a 5 or a 10 M_J companion could be detected for each of our survey stars is shown in Table 6. Using the Baraffe et al. (2003) COND models, for our top 15 stars, we detect no 5 M_J planets at separations larger than 24.3 AU and no 10 M_J planets at separations larger than 9.25 AU. While these numbers are comparable to those found in Masciadri et al. (2005), our current survey actually attains higher contrasts on a case-by-case basis than Masciadri et al. (2005). Our median survey object has an age of 30 Myr and a K spectral type, whereas the median survey object of Masciadri et al. (2005) has a considerably younger age of 12 Myr and an M spectral type; the star-planet contrast is less at younger ages. Thus one would expect a younger object to have a lower minimum separation at a given attained contrast than a similar but older object and similarly, a later spectral type object to have a lower minimum separation at a given attained contrast than an earlier spectral type object with a similar age. For the 10 objects in common between the surveys, our survey attains lower minimum separations for 6 out of 10 objects and comparable separation for 2 others (we note also that the two objects for which we did not attain lower separations were particularly low quality SDI data sets). Minimum detectable separations for a 5 M_J object for the 10 objects in common are plotted in Figure 16 (using the ages

TABLE 5
Limiting H Magnitude (5 σ) at 1.0″

Object	ΔF1	Separation (AU)	ΔH (T8 SpT)	m_H	M_H
ϵ Eri	11.3 ± 0.2	3.22	12.2	14.1	16.6
ϵ Ind A	12 ± 0.16	3.63	12.9	15.2	17.4
HD 201091	9.42 ± 0.05	3.48	10.3	12.8	15.1
HD 114613	7.24 ± 0.13	20.5	8.11	11.5	9.94
HD 17925	11.3 ± 0.19	10.4	12.2	16.4	16.3
HD172555A	11.2 ± 0.098	30	12.1	16.4	14
π_1 UMa	9.28 ± 0.14	14.3	10.1	14.4	13.6
HD 48189A	9.87 ± 0.24	21.7	10.7	15.4	13.7
GJ803	10.7 ± 0.03	9.94	11.6	16.4	16.4
AB Dor	11 ± 0.17	14.9	11.9	16.7	15.8
HD 155555AB	7.3 ± 0.046	30	8.17	13.1	10.7
GJ 417	8.44 ± 0.05	21.7	9.31	14.3	12.6
HD 181321	8.63 ± 0.048	20	9.5	14.6	13.1
SRX 1	11.2 ± 0.13	23.5	12.1	17.3	15.4
GJ 799A	9.55 ± 0.14	10.2	10.4	15.6	15.6
DX Leo	9.98 ± 0.039	17.7	10.8	16	14.8
GJ 862	10.7 ± 0.12	15.4	11.6	16.9	16
V834 Tau	10.2 ± 0.18	13.5	11.1	16.4	15.7
HD 166435	9.98 ± 0.061	25.2	10.8	16.2	14.2
LQ Hya	11 ± 0.035	18.3	11.9	17.5	16.2
HD 186704	7.35 ± 0.052	30.3	8.22	13.8	11.4
HD 92945	10.8 ± 0.062	21.6	11.7	17.5	15.8
UY Pic	11.5 ± 0.033	23.9	12.4	18.3	16.4
HD 224228	10.8 ± 0.11	22.1	11.7	17.7	16
EK Dra	8.86 ± 0.14	33.9	9.73	15.7	13
HIP 1481	10.8 ± 0.046	41	11.7	17.9	14.8
CD −64 1208	9.88 ± 0.54	29.2	10.8	17.1	14.8
HD 135363	8.65 ± 0.025	29.4	9.52	15.8	13.5
HIP 23309	10 ± 0.051	26.3	10.9	17.3	15.2
GJ 182	10.2 ± 0.15	26.7	11.1	17.6	15.5
V577 PerA	10 ± 0.062	33.8	10.9	17.4	14.8
HIP 9141	10.5 ± 0.028	42.4	11.4	18	14.9
HIP 30030	8.3 ± 0.09	52.4	9.17	15.8	12.2
KW Lup	9.86 ± 0.17	40.9	10.7	17.3	14.2
ERX 8	10.7 ± 0.12	37.1	11.6	18.5	15.7
ERX 6	10.6 ± 0.12	49.3	11.5	18.4	14.9
AO Men	7.9 ± 0.015	38.5	8.77	15.8	12.9
AB Pic	10.8 ± 0.013	45.5	11.7	18.8	15.5
GJ 207.1	8.74 ± 0.089	16.8	9.61	16.8	15.7
HIP 112312A	10.6 ± 0.068	23.6	11.5	18.7	16.8
BD +05 378	9.52 ± 0.074	40.5	10.4	17.6	14.6
TWA 25	10.5 ± 0.18	44.1	11.4	18.9	15.7
RX J1224.8−7503	8.04 ± 0.16	24.2	8.91	16.8	14.9
HD 155555C	10.8 ± 0.043	30	11.7	19.6	17.2
TWA 14	8.74 ± 0.047	66.7	9.61	18.3	14.2

adopted by Masciadri et al. [2005]). Our survey is generally more sensitive than Masciadri et al. (2005) on shared stars because the SDI technique allows us to achieve higher contrasts closer to the star (separations of 0.3″ −1.0″) compared to the deep broadband imaging technique of Masciadri et al. (2005), thus allowing us to potentially detect companions at tighter separations. We also shared four survey objects in common with Lowrance et al. (2005) and one object (ϵ Eri) in common with Luhman & Jayawardhana (2002). In all of these cases, our limiting contrasts at 0.5″ ($\Delta H \sim$ 10–11 mag) are considerably higher than those attained in these previous surveys ($\Delta H \sim$ 6.5–7.6 mag); thus, we are sensitive to planets at much smaller separations with SDI.

3.4. *Survey Completeness*

One would not expect a planet to be detectable at all phases of its orbit. To really understand the types of planets to which we are sensitive, we must take orbital motion into account and translate separations on the sky into orbital semimajor axes (a). To this end, we generated contour plots of fractional completeness as a function of mass and semimajor axis. For every survey star, we simulate 10,000 planets for each combination of mass and semimajor axis. Eccentricities are drawn from a distribution of eccentricities consistent with known radial velocity planets. Standard distributions were used to randomly compute viewing angle and orbital phase, giving an instantaneous separation between star and planet. We use the distance, age, spectral type, and H-band magnitude of the star, and luminosity as a function of mass, calculated from the Burrows et al. (2003) models, to provide each simulated planet with a separation on the sky in arcseconds and an H-band flux ratio compared to its parent star. Combining this with the SDI contrast curve for each star in the survey, we can then determine the percentage of simulated planets detected as a function of mass

TABLE 6

Star/Planet Projected Minimum Detectable Separations for 5 and 10 M_J Planets

Object	Age (Myr)	Distance (pc)	Separation 5 M_J (AU)	Separation 10 M_J (AU)
AB Dor	70	14.94	20.62	10.01
AO Men	12	38.48	...	23.85
BD +05 378	12	40.54	30.00	10.54
CD −64 1208	12	34.21	24.29	9.24
DX Leo	115	17.75	...	25.02
EK Dra	70	33.94	...	...
ϵ Eri	800	3.22	...	...
ϵ Ind A	1300	3.63	...	5.91
GJ 174	160	13.49	...	15.24
GJ 182	12	26.67	17.87	5.87
GJ 207.1	100	16.82	...	12.28
GJ 417	115	21.72	...	...
GJ 799A	12	10.22	4.70	1.74
GJ 799B	12	10.22	3.17	1.64
GJ 803	12	9.94	2.78	1.09
GJ 862	6300	15.45	...	...
HD 114613	4200	20.48	...	...
HD 128311	630	16.57	...	...
HD 135363	3	29.44	13.54	9.42
HD 155555 AB	12	30.03	...	...
HD 155555 C	12	30.03	3.30	3.30
HD 166435	100	25.24	...	...
HD 172555 A	12	29.23	32.45	19.58
HD 17925	115	10.38	19.52	8.30
HD 181321	160	20.86	...	...
HD 201091	2000	3.48	...	...
HD 224228	70	22.08	47.92	12.15
HD 45270	70	23.50	51.00	15.51
HD 48189 A	70	21.67	...	26.44
HD 81040	2500	32.56	...	...
HD 8558	30	49.29	69.00	22.18
HD 186704	200	30.26	...	...
HD 9054	30	37.15	34.92	9.29
HD 92945	70	21.57	43.14	9.71
HIP 112312 A	12	23.61	5.43	3.31
HIP 1481	30	40.95	59.38	20.88
HIP 23309	12	26.26	16.28	5.51
HIP 30030	30	52.36	...	129.84
AB Pic	30	45.52	40.05	13.20
HIP 9141	30	42.35	78.78	22.45
KW Lup	2	40.92	8.59	6.14
LQ Hya	13	18.34	5.32	2.94
RX J1224.8−7503	16	24.17	19.34	4.83
TWA 14	10	66.67	32.00	12.00
TWA 25	10	44.05	14.98	9.25
UY Pic	70	23.87	28.64	7.40
V577 Per A	70	33.77	...	23.64
π_1 UMa	210	14.27	...	...

Note.—The ellipses mean that such an object is too low in mass to be detected with our current survey contrast level for that star.

and semimajor axis for each survey star. Contour plots for a set of four typical program stars (AB Dor, DX Leo, GJ 182, and GJ 799B) are presented in Figure 17. Note that we conservatively assume only T-type objects can be detected; hence, masses $>10\ M_J$ are not considered for many young targets. The value attached to each contour level defines the completeness of our observation to detecting (at the 5 σ confidence level) a planet with the given semimajor axis and mass. It is worth noting that the only assumptions necessary for the generation of these plots is the eccentricity distribution of planets and the Baraffe et al. (2003) COND models.

We use this method to summarize our survey completeness in Figure 18. Having computed the completeness for each star to planets at various masses and semimajor axes, we take slices at representative values of the semimajor axis and present the number of stars in our 54 star survey which are at least 50% complete to such a planet. Our survey places the strongest constraints on planets between 4 and 8 M_J with semimajor axes between 20 and 40 AU. With 20 such stars (with 50% or greater completeness in this mass/semimajor axis range) surveyed without a detection of a planet, a simple way of interpreting our results (although without

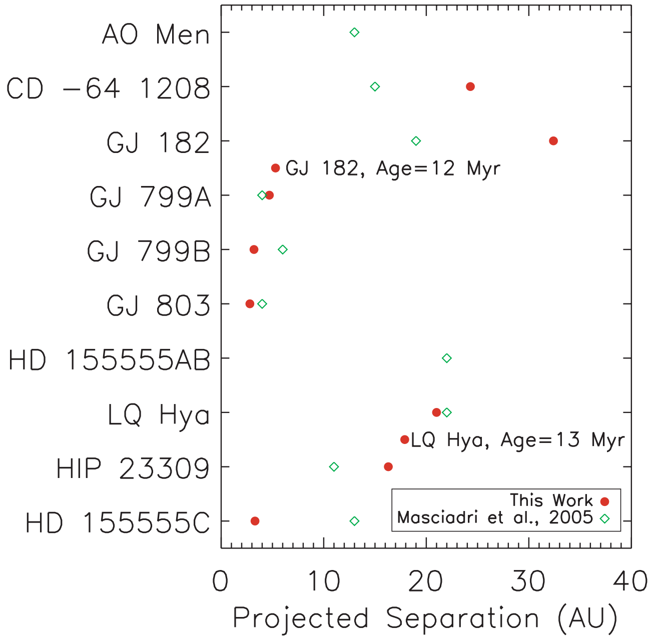

FIG. 16.—Minimum detectable planet separations for a 5 M_J planet for the 10 objects in common between this survey and Masciadri et al. (2005), who used VLT NACO without SDI. For the purpose of comparison, we have adopted ages from Masciadri et al. (2005); we note our preferred age on the figure where our adopted ages differ from Masciadri et al. (2005). We translated theoretical 5 M_J planet models (Baraffe et al. 2003) into H magnitudes for these 10 cases and then determined the minimum separation at which such a companion could be detected (at the 5 σ level) in our survey. For the 10 objects in common between the surveys, our SDI survey attains lower minimum separations for 8 out of 10 objects and comparable separations for two others (we note also that the two objects for which we did not attain lower separations were particularly low quality AO/SDI data sets).

statistical rigor) is that we would expect the frequency of such planets to be of order 10% or less.

The evolutionary models of Burrows et al. (2003) and Baraffe et al. (2003) use a "hot start" initial condition which, while appropriate for brown dwarfs, is possibly significantly different from the actual initial origins of planets. The Burrows et al. (2003) models begin with a high-temperature, high-entropy hydrogen-helium sphere which is allowed to radiate and cool over time. In contrast, a planet forms when gas accretes onto a rocky core, according to the core-accretion models of Ida & Lin (2005) and the disk instability models of Boss (2003). Recently, Marley et al. (2006) simulated model planets with more realistic (lower entropy) initial conditions. These model planets have significantly lower luminosities at young ages (<1 Gyr). Model planets also converge to the hot-start evolutionary tracks at different times according to mass: a 1 M_J model converges to traditional tracks by 20 Myr, while a 10 M_J model requires up to 1 Gyr to match traditional tracks. Currently, H-band magnitudes for these models are not yet available but will be available in fall 2007/winter 2008 (J. Fortney 2007, private communication). When H-band magnitudes are available, we will repeat this analysis using these new models.

3.5. *Sensitivity Case Study: AB Dor with Simulated Planets*

Since our survey data are highly saturated in the core of the image, it is difficult to place simulated objects in our data with a high degree of positional accuracy, as there is no external reference for position between data taken at different dithers and roll angles. However, as part of the SDI survey observations, our team discovered a close-in (0.156″) companion (hereafter AB Dor C) to the young star AB Dor (Close et al. 2005b). While this companion is a very low mass M star (0.090 ± 0.005 $M_\odot$, M5.5 ± 1; Close et al. 2005b, 2007b) and, hence, does not possess methane absorption features, it is still clearly detected in our SDI data. In our second AB Dor data set where AB Dor C is separated from its primary by 0.2″ (Nielsen et al. 2005), the AB Dor C source can be used to our advantage as a reference position from which to offset, allowing us to add simulated planets into this data set with highly accurate positions and relative fluxes independent of our "pipeline"-calculated centroids.

Simulated planets were produced by scaling ∼10 × 0.1 s unsaturated images of AB Dor A taken right before the example data set. Planets were simulated with $\Delta F1(1.575\ \mu m) = 9$, 10, 11, and 12 mag and with methane-break strengths appropriate for T5, T6, and T8 spectral types. Methane-break strengths were calculated using the methane spectral index defined in § 3.2. Photon noise and zero points appropriate for each object were added using the IRAF `artdata/mkobject` tool. The photometric zero point was calculated from AB Dor C.

A fully reduced, 28 minute data set of AB Dor A (70 Myr K1 V at a distance of 14.98 pc, $V = 6.88$) from the VLT SDI device is presented in Figure 19 with simulated planets added at separations of 0.4″, 0.6″, 0.8″, 1.0″, 1.2″, 1.4″, 1.6″, 1.8″, 2.0, and 2.2″ from the primary [$\Delta F1(1.575\ \mu\text{m}) = 9$, 10, 11, and 12 mag and spectral type T8]. Past 0.7″, the $\Delta F1(1.575\ \mu\text{m}) = 10$ simulated planets are detected with $S/N > 10$. The 2.2″ object falls off the edge of the aperture in several dithers and thus appears somewhat attenuated compared to the other simulated objects. Maximum achievable companion contrast at the 5 σ level as a function of distance from the star is plotted in Figure 20. The residual noise curve for this star (see § 3.3) is also overplotted. Contrast curves (5 σ) calculated with both techniques agree well with each other. Using the magnitude offsets developed in § 3.4, we convert our $\Delta F1(1.575\ \mu\text{m})$ contrasts into ΔH for each spectral type. We adopt $\text{Offset}_A = 0$ mag and $\text{Offset}_B = 0.5$ mag for a T5 object, $\text{Offset}_B = 0.6$ mag for a T6 object, and $\text{Offset}_B = 0.87$ mag for a T8 object. The ΔH versus separation in arcseconds is presented in Figure 21.

The $\Delta F1$ contrasts were translated into planet masses using the 100 Myr COND models of Baraffe et al. (2003). According to the 100 Myr old model, objects with mass ≤10 M_J will have $T_{\text{eff}} < 900$ K; these objects are reliably of spectral types later than T7 (temperature scale from Burgasser et al. [2003]). Thus, we adopt the T8 spectral-type curve for this analysis. AB Dor has a likely age of 50–70 Myr (Nielsen et al. 2005; Close et al. 2007b); we interpolate the COND models of Baraffe et al. (2003) to derive masses at these ages as well. The minimum detectable planet mass as a function of distance from the star is plotted in Figure 22. Adopting an age of 70 Myr for AB Dor A, we can detect a 7 M_J planet 12 AU from the star. However, as noted above, the Baraffe et al. (2003) models use a hot-start initial condition which may be inappropriate for a young planet. The Marley et al. (2006) models use more appropriate initial conditions and when H-band magnitudes become available for these models, we will repeat this analysis.

3.6. *Comparison with Other Direct Detection Methods*

We believe that our SDI images are the highest contrast astronomical images ever made from ground or space for methane-rich companions ≤ 1″ from their star. To substantiate this claim, we compare our SDI contrast curves with those produced using a variety of other competing methods (Azimuthal Differential Imaging [ADI], Marois et al. 2006; Lyot coronagraph, Hinkley et al. 2007; *HST* NICMOS, G. Schneider et al. 2003, unpublished; K-band Keck AO, G. Schneider et al. 2003, unpublished; and

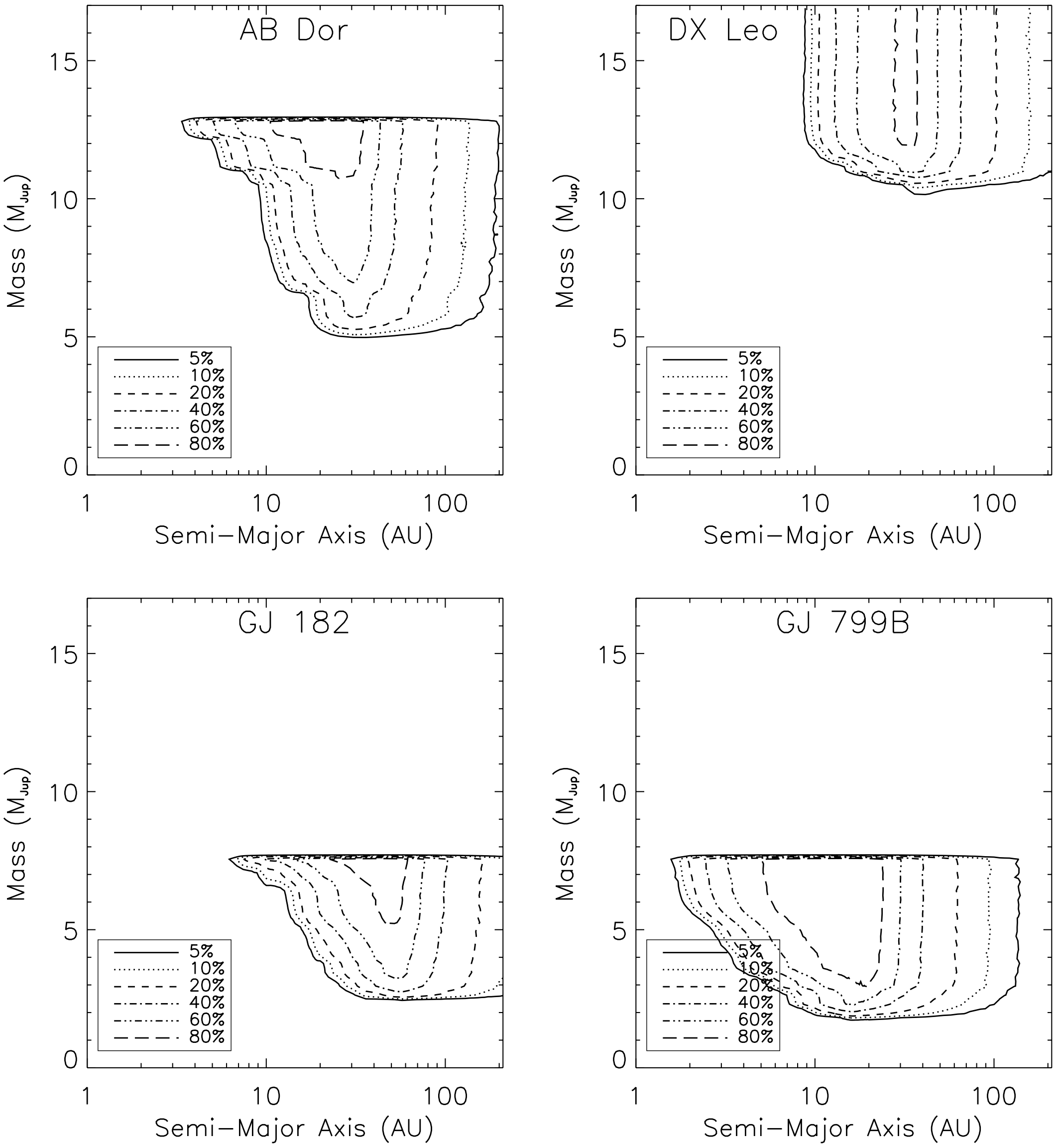

FIG. 17.—Planet detection completeness contour plots for a set of four typical program stars (*upper left*, AB Dor; *upper right*, DX Leo; *lower left*, GJ 182; *lower right*, GJ 799B). For a given mass and semimajor axis, 10,000 planets are simulated by our Monte Carlo method, over the expected distributions of eccentricity, orbital phase, and viewing angle. Given the parameters of the target star and the COND models of Baraffe et al. (2003), we determine what fraction of the simulated planets are detectable at the 5 σ level given the contrast plot for that star. The contours show this detection probability across the 100,000 different combinations of mass and semimajor axis considered in this plot. The strong upper limit in mass is set by our conservative <1400 K limit for the methane break required for a robust SDI detection. In these models, we simply do not allow an object with $T_{\rm eff}$ > 1400 K to be detected, when in reality SDI can detect such nonmethane objects (e.g., AB Dor C; Close et al. 2005b; Nielsen et al. 2005). For a complete set of planet detection completeness contour plots, see http://exoplanet.as.arizona.edu/~lclose/SDI.html.

NACO deep imaging in the K_s band, Masciadri et al. 2005). Comparison contrast curves are presented in Figure 23. Apart from the Lyot and NICMOS curves, all curves are from ≥8 m class telescopes. For ease of comparison, we convert our ΔF1 = 1.575 μm SDI contrast curve into the equivalent ΔH contrast appropriate for T8 and Y spectral type companions. For methanated companions, SDI provides improved contrast by 1–4 mag within 1″ compared to other methods.

3.7. *New and Confirmed Close Binary Stars*

A number of close binary stars were discovered or confirmed during our survey. In Table 7, we present separations and PAs measured from unsaturated SDI images of these stars acquired before each full SDI data set was taken. These values are meant as estimates; hence, no error estimate is provided. We discovered close stellar companions to HIP 9141 (0.15″ measured SDI separation), AB Dor A (0.16″ measured SDI separation, see Close et al. 2005a), HD 48189A (0.14″ measured SDI separation), HD 135363 (0.26″ measured SDI separation), and CD −64 1208 (0.18″ measured SDI separation). The <0.5″ separation between the primary stars and these object makes it highly improbable that they are background objects. In addition, we confirmed the close binary RX J1243.6−7834 (0.068″ measured SDI separation) discovered by Brandner et al. (2000), the visual double LH 98 062 (2.4″ measured SDI separation) discovered by Mochnacki et al. (2002), the spectroscopic binary TWA 4 (0.78″ measured SDI separation) discovered by Torres et al. (1995), and the close binary EK Dra (0.67″ measured SDI separation) discovered by Metchev & Hillenbrand (2004).

3.8. *Candidate Identification/Elimination*

Survey data were examined for planet candidates by eye and also using automated detection algorithms; generally, the human eye proved more effective for detecting candidates. We identified

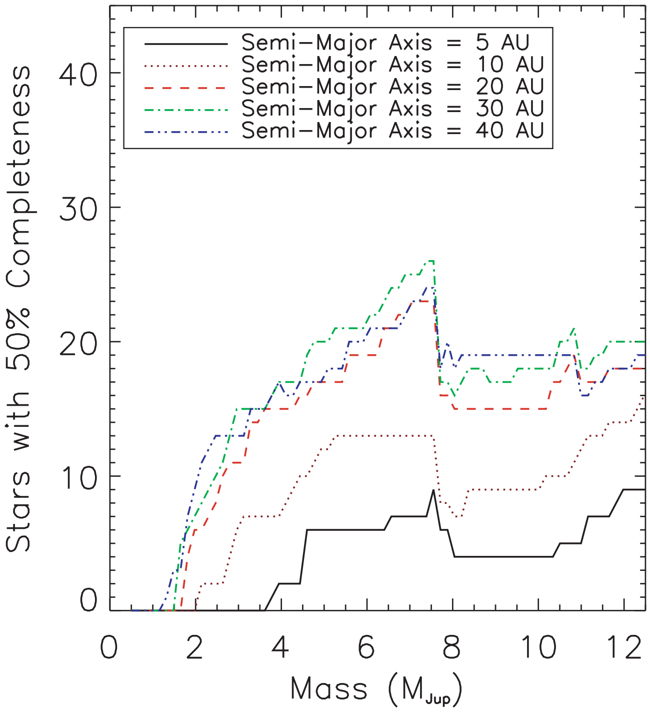

FIG. 18.—Our 50% completeness levels. Combining the results of Fig. 17, we consider individual values of the semimajor axis across the planetary mass range and at each combination calculate the total number of stars in our survey (out of a total of 54) where the fraction of such planets, given by the Monte Carlo simulation, that can be detected at the 5 σ level is 50% or greater. *Clearly, our survey is best able to place constraints on planets between 4 and 8 M_J and with semimajor axis between 20 and 40 AU.* The decrease in sensitivity for masses > 8 M_J is due to the fact that such high-mass planets are too hot to possess significant methane absorption if they are very young and, thus, are not ideal SDI targets. The higher completeness for 4–8 M_J planets for semimajor axis of 30 AU vs. semimajor axis of 40 AU is due to the small field of view of the SDI device; planets with semimajor axes > 30 AU can fall outside the SDI field in some of these cases.

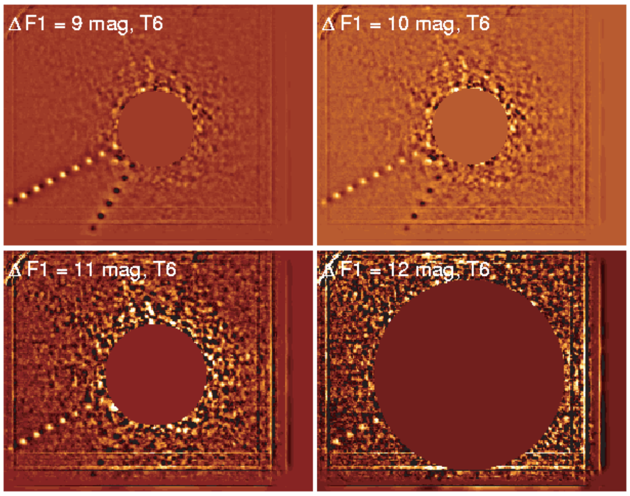

FIG. 19.—Complete reduced data set of AB Dor A (28 minutes of data at a series of rotator angles: 0°, 33°, 33°, 0°) from the VLT SDI device. Simulated planets have been added every 0.2″ from the star (0.4″, 0.6″, 0.8″, 1.0″, 1.2″, 1.4″, 1.6″, 1.8″, 2.0″, and 2.2″) with ΔF1(1.575 μm) = 9 mag (*upper left*, attenuation in magnitudes in the 1.575 μm F1 filter), 10 mag (*upper right*), 11 mag (*lower left*), and 12 mag (*lower right*) fainter than the star. The 0.4″ object falls within the inner dark circle (dark circle radius of 0.5″, 0.5″, 0.7″, and 1.3″, respectively, for the 9, 10, 11, and 12 mag objects); the 2.2″ object falls outside the frame aperture in a number of dither images and thus is detected with lower S/N than the other objects. These simulated planets are scaled from unsaturated images of AB Dor A taken right before the example data set (and have fluxes and photon noise in each filter appropriate for a T6 object).

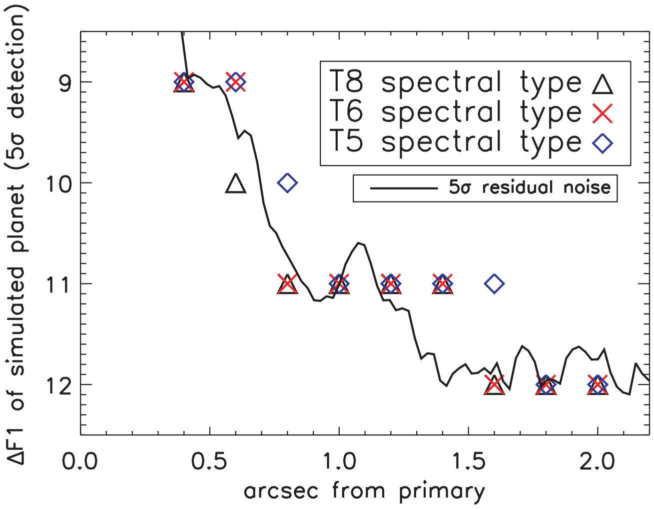

FIG. 20.—Maximum achievable planet contrast (5 σ detection) vs. separation for 28 minutes of VLT SDI data for AB Dor A. To determine the maximum achievable planet contrast as a function of separation, we inserted and then attempted to retrieve simulated planets with a variety of separations and ΔF1 contrasts appropriate for T5, T6, and T8 spectral types. The residual SDI noise curve for AB Dor A is also overplotted; the two curves agree well, giving us confidence in our measured contrast limits.

eight very tentative planet candidates at the VLT which passed the following tests:

1. Candidate must appear at the appropriate positions in the full reduced data (i.e., candidate image position must jump by the appropriate roll angle).
2. Candidate must appear (at least marginally) at the appropriate position in each of the separate roll angle images.
3. Candidates detected in the F1(1.575 μm) – F3a(1.625 μm) difference should also be detected in the F2(1.6 μm)–F3a(1.625 μm) difference as well.

These extremely tentative (<2 σ) candidates are noted in the comments column of Table 1, with the predicted mass (from the

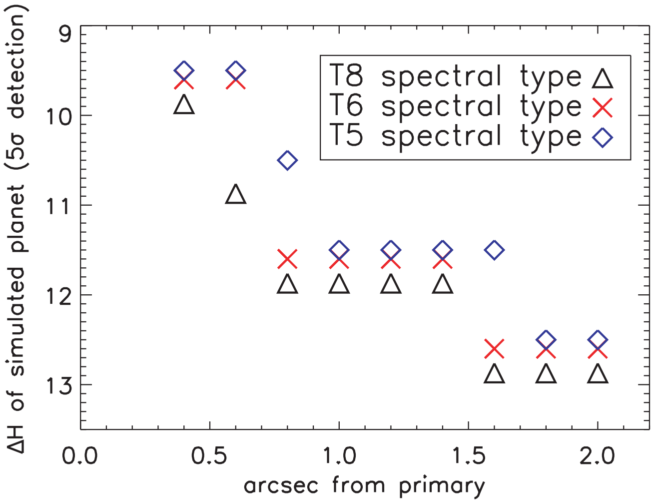

FIG. 21.—Maximum achievable *H*-band planet contrast (5 σ detection) vs. separation for 28 minutes of VLT SDI data for AB Dor A. To determine the maximum achievable planet contrast as a function of separation, we inserted and then attempted to retrieve simulated planets with a variety of separations and ΔF1 contrasts appropriate for T5, T6, and T8 spectral types. The ΔF1 contrasts were converted to Δ*H* magnitudes using the magnitude offsets calculated in § 3.3.

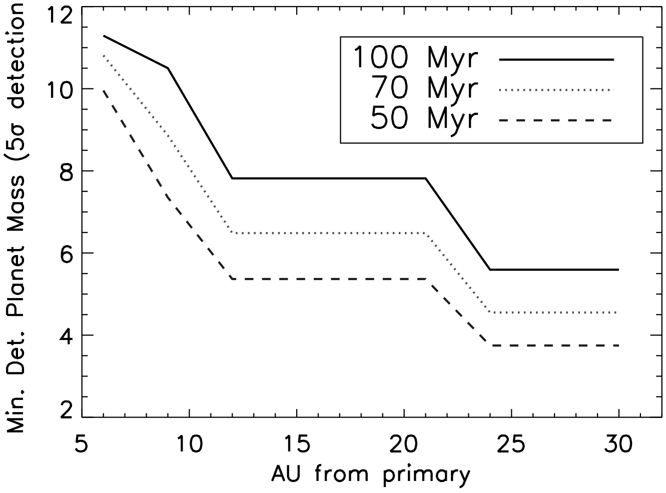

Fig. 22.—Minimum detectable planet mass (5 σ detection) vs. separation (AU) for 28 minutes of VLT SDI data for AB Dor A. To determine the minimum detectable planet mass as a function of separation, we inserted and then attempted to retrieve simulated planets with a variety of separations and ΔF1 contrasts appropriate for T5, T6, and T8 spectral types. The ΔF1 contrasts were converted to ΔH magnitudes using the magnitude offsets calculated in § 3.3 and were then converted to absolute H magnitudes using the 2MASS apparent H magnitude and the *Hipparcos* distance for each star. Absolute H magnitudes were converted into planet masses using the COND models of Baraffe et al. (2003) and adopting a range of system ages from 50 to 100 Myr. For AB Dor, we should be able to image (5 σ detection) a 7 $M_{\rm J}$ planet 12 AU from the star. For a complete set of minimum detectable planet mass vs. separation curves, see http://exoplanet.as.arizona.edu/~lclose/SDI.html. [*See the electronic edition of the Supplement for a color version of this figure.*]

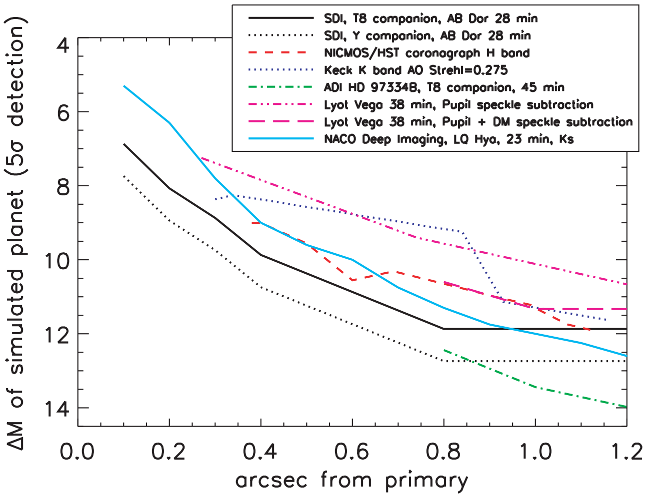

Fig. 23.—Comparison of SDI contrast curve with other methods. The Lyot curve is for the 3.6 m Advanced Electro-Optical System telescope (Hinkley et al. 2007), and the NICMOS curve coronograph curve is from *HST* (G. Schneider et al. 2003, unpublished); otherwise curves are all from $\geq$8 m class telescopes. We use the LQ Hya contrast curve from Masciadri et al. (2005) because this star (K2, 18 pc vs. K1, 15 pc) is the closest match from that work to AB Dor A (our SDI comparison star). The SDI contrast curve has been converted from ΔF1 = 1.575 μm to ΔH contrasts appropriate for T8 and Y spectral type objects. Inside 0.4″, SDI contrasts are derived from the one-trajectory SDI contrast plot of AB Dor A; outside of 0.4″, SDI contrasts are derived from our in-depth planet simulation case study of AB Dor A. For methanated companions, SDI provides improved contrast by 1–4 mag within 1″ compared to other methods. Past 1″, narrowband imaging becomes less efficient, and broadband techniques (such as ADI; Marois et al. 2006) reach higher contrasts.

models of Burrows et al. [2003]) and separation had it been real. No candidates were detected with >3 σ. None of the eight tentative candidates were detected at a second epoch; thus, the survey reached a null result for extrasolar planets at the ~3 σ level and certainly at the 5 σ level analyzed here.

3.9. *Planet Detectability*

To determine what sort of planets we can detect in this survey, we converted our contrast curves in Δmag units into minimum detectable mass versus separation (assuming a late T to early Y spectral type for all possible objects and using the models of Burrows et al. [2003]). We calculated minimum detectable mass versus separation for all stars with contrast curves in Figures 8–14; minimum detectable mass versus separation is presented for a set of four typical survey stars (AB Dor, DX Leo, GJ 182, and GJ 799B) in Figure 24. However, to detect an object of any given mass requires that such an object exists around its parent object. The likelihood of detecting any object at a given radius is a combination of the minimum detectable mass for the parent star at that radius and the likelihood of such an object existing. Therefore, it is very important to fully characterize and understand the expected distribution of objects around each survey star. The results of the survey then also constrain the possible distribution of extrasolar planets as a function of radius.

To this end, we ran detailed Monte Carlo simulations to characterize the ensemble of planets expected to exist around each star. We conduct a similar simulation to that used to produce the contour plots of Figure 17, as described in § 3.4 (these simulations are described in much more depth in Nielsen et al. [2006]). In contrast to the production of the contour plots, we simulate 10^6 planets instead of 10^4, and mass and semimajor axis are now assigned distributions of their own. The mass and semimajor axis distributions, like the distribution for eccentricity, are produced by considering the population of published radial velocity planets (e.g., Butler et al. 2006), with mass and eccentricity both chosen to fit the histograms from observed planets. Semimajor axis has been observed to follow a distribution of $N(a) \propto a^{-1}$ for radial velocity planets (Wright et al. 2005). Since the radial velocity method has an inherent bias toward close-in planets (which have shorter orbital periods and larger radial velocity amplitudes), we attempt to correct for this by assuming a power-law distribution that is constant in semimajor axis, i.e., $N(a) \propto$ constant. We consider the results of Fischer & Valenti's (2005) volume-limited sample and choose an outer limit for the semimajor axis distribution such that, for stars in the metallicity range in our sample, each star is expected to host one planet. This is done by integrating the semimajor axis distribution from 0.02 AU (corresponding to HD 41004Bb, the closest-in exoplanet known thus far) to 2.5 AU, the detection limit for the sample of Fischer & Valenti (2005), then noting the fraction of stars with planets in the metallicity range ($-0.5 < [{\rm Fe/H}] < 0.25$) of our target stars (4.1%), and choosing an upper cutoff to the distribution when the integral reaches 100%. This gives us a constant probability distribution for semimajor axis between 0.02 and 45 AU that contains the same number of planets found in the <2.5 AU radial velocity survey.

The ensemble of simulated planets is shown for our set of four typical stars in Figure 24. Simulated planets which are detected are plotted as blue dots, and those that remain undetected are plotted as red dots. In addition to the contrast plot, we also consider a planet "undetectable" when its apparent H magnitude drops below 21 mag (a limit set by our total integration time) or when the planet's temperature rises above 1400 K (given as a function of age and planet mass by Burrows et al. [2003]). Above this temperature, the strength of the 1.62 μm methane

TABLE 7
Binary Properties

Object	Separation (arcsec)	Position Angle (deg)	Est. ΔF1	Epoch
SDI Survey Discoveries				
AB Dor AC[a]	0.16	127	$\Delta K_s = 9.45 \pm 0.1$	2004 Feb 02
	0.2			2004 Sep 28
				2004 Nov 16
HIP 9141	0.15	355	∼0.1	2004 Sep 27
HD 48189AC	0.14	143	1.5	2004 Nov 17
HD 135363	0.26	132	1.7	2005 May 01
CD −64 1208	0.18	95	2.8	2004 Sep 16
SDI Survey Confirmations				
RX J1243.6−7834[b]	0.068	171/351	∼0	2004 Feb 02
LH 98 062	2.4	354	∼0	2004 Feb 03
TWA 4	0.78	3	0.05	2004 Feb 02
EK Dra	0.67	176	3.0	2005 May 01

[a] Separation and position angle from Close et al. (2005b). For updated photometry and astrometry see Close et al. (2007b).

[b] As RX J1243.6−7834 is nearly an equal-magnitude binary, we were unable to determine which star was the primary (as selected by Brandner et al. 2000) and thus present two values for the position angle (assuming each star is the primary in turn).

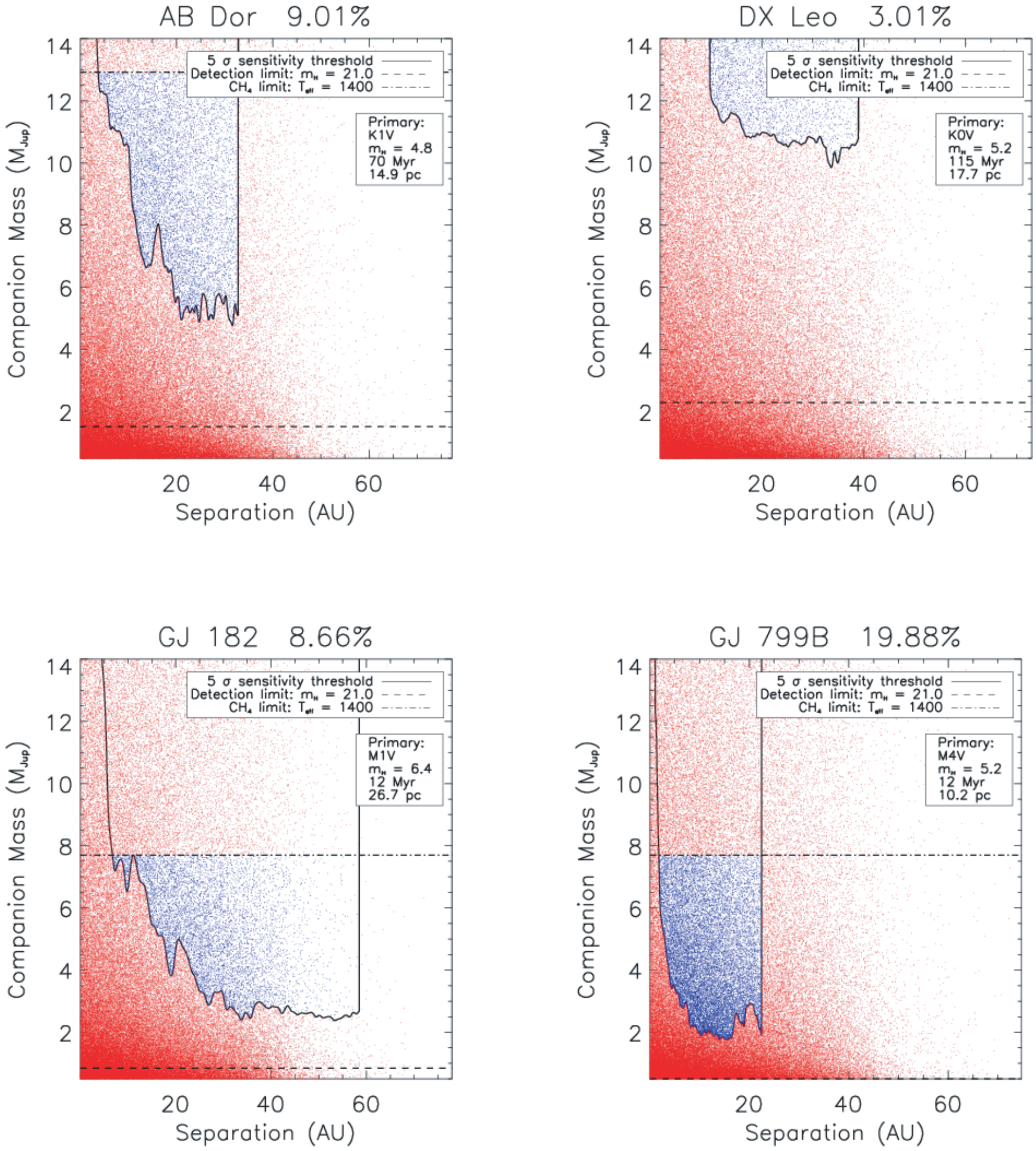

FIG. 24.—Minimum detectable mass vs. separation for a set of four typical program stars (*upper left*, AB Dor; *upper right*, DX Leo; *lower left*, GJ 182; *lower right*, GJ 799B). We convert our contrast curves in Δmag units (from Figs. 8–12) into minimum detectable mass vs. separation (in AU) using the models of Burrows et al. (2003) and the distance to the star. To characterize the possible planets we expect to detect around each star, we simulated an ensemble of 10^6 possible planets per star, assuming distributions for mass, eccentricity, and semimajor axis based on known radial velocity planets, as well as distributions for orbital phase and viewing angle. When combined with the properties of the individual target star and its measured contrast curve, we can determine what fraction of these simulated planets we expect to detect at the 5 σ level (shown above each plot with the name of the target star). The ensemble of simulated planets is shown as small dots for each star; simulated planets which are detected with the contrast attained by SDI are plotted in blue, and those that remain undetected are plotted in red. Assuming each star possesses exactly one planet, we can assign a detection probability for that star from the percentage of simulated planets detected. For our 48 program stars which possess contrast curves, the average detection probability is 4.6%, the median detection probability is 3.5%, and the maximum detection probability is 33%. For GJ 799B (12 Myr M star at 10 pc), we can detect (at 7.8 σ) a 5 M_J planet at 2 AU.

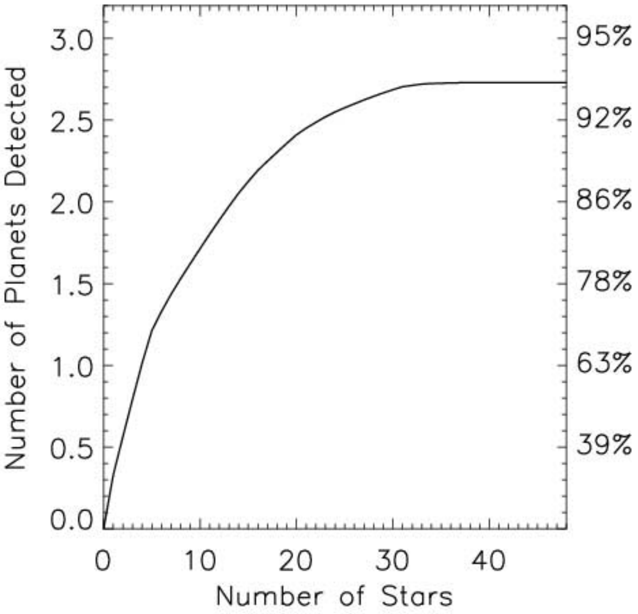

FIG. 25.—Expected number of planets detected. By taking the results of our Monte Carlo simulations and assuming that each program star possesses exactly one planet, we can assign a detection probability for that star from the percentage of simulated planets detected. By adding these detection fractions for each star, we can compute the expected number of planets detected from our survey. We order the target stars by decreasing detection probability and plot the total number of planets expected to be detected as a function of the number of stars. Over the entire survey, we expect to detect 2.73 planets. Thus, our assumed distribution for the frequency (one planet per star, hence 100%), semimajor axis distribution [$N(a) \propto$ constant], and luminosities (Burrows et al. 2003) of extrasolar planets is excluded at the 93% level by our extrasolar planet survey null result.

break weakens to the point that the SDI method loses effectiveness. Since we assume that each program star possesses exactly one planet that follows the distributions given above, we can assign a detection probability for that star from the percentage of the simulated planets that are detectable at the 5 σ level. For our 48 program stars (consisting of 40 stars with ages $>$ 250 Myr and closer than 50 pc, one 10 Myr old star at a distance of 67 pc, three stars with known radial velocity planets, and four nearby solar analogs) which possess contrast curves, the average detection probability is 4.6%, the median detection probability is 3.5%, and the maximum detection probability is 33%. We have chosen to leave the older stars in this sample in our statistics even though their detection probabilities are essentially zero. Integrating over the probability distribution of our program stars, in Figure 25 we plot the number of planets we expect to detect as a function of total stars observed, ordering the results so that the best stars (highest detection probabilities) are considered first. For the 48 stars in our surveys for which we acquired contrast curves, we expect to detect a total of two to three planets (2.73 to be exact) based on the above assumptions. Thus, our survey null detection rules out this exoplanet distribution at the 93% level. It is important to note that this null result shows that this particular combination of assumptions (mass distribution, eccentricity distribution, constant semimajor axis distribution, upper limit to semimajor axis at 45 AU, assumption that each star has a planet, and the mass-luminosity conversion from the COND models of Baraffe et al. [2003]) is ruled out to this confidence level; determining which individual assumptions are incorrect will required data beyond that of the current survey. These simulations (including a variety of other possible exoplanet distributions) are discussed in more detail in Nielsen et al. (2007). Nevertheless, our null detection in this survey sets strong upper limits on the distribution of young massive extrasolar planets >5 AU from their primaries and provides valuable constraints for theories of planet formation and migration.

4. CONCLUSIONS

We obtained data sets for 54 stars (45 stars were observed in the southern sky at the VLT, 11 stars were observed in the northern sky at the MMT, and two stars were observed at both telescopes). In our VLT data, we achieved *H*-band contrasts of >10 mag (5 σ) at a separation of 1.0″ from the primary star on 45% of our targets and *H*-band contrasts of >9 mag at a separation of 0.5″ on 80% of our targets. With this degree of attenuation, we should be able to image (5 σ detection) a 7 $M_{\rm J}$ planet 15 AU from a 70 Myr K1 star at 15 pc or a 7.8 $M_{\rm J}$ planet at 2 AU from a 12 Myr M star at 10 pc. We believe that our SDI images are the highest contrast astronomical images ever made from ground or space for methane-rich companions within 1″ of their primary star.

Eight tentative candidates were identified (none with S/N $>$ 2 σ). Had these candidates been real, they would have possessed separations of 3–15.5 AU and masses of 2–10 $M_{\rm J}$. However, none of the candidates were detected in second-epoch observations. Thus, we find a null result from our survey. Nonetheless, our result still has serious implications for the distribution of extrasolar planets. In the course of our survey, we also discovered five new close stellar binary systems with measured separations of 0.14″ –0.26″.

For 20 of our survey stars, we attained 50% completeness for 4–8 $M_{\rm J}$ planets at semimajor axes of 20–40 AU. Thus, our completeness levels are sufficient to significantly test theoretical planet distributions. From our survey null result, we can rule out (at the 93% level) a model planet population using a constant distribution [$N(a) \propto$ constant] of planet semimajor axis out to a distance of 45 AU (a number of further exoplanet distribution models are considered in E. Nielsen et al. [2007, in preparation]). Our null detection in this survey sets strong upper limits on the distribution of young massive extrasolar planets >5 AU from their primaries and provides valuable constraints for theories of planet formation and migration.

This publication is based on observations made with the MMT and the ESO VLT at Paranal Observatory under programme IDs 074.C-0548, 074.C-0549, and 076.C-0094. This publication makes use of data products from the Two Micron All Sky Survey, which is a joint project of the University of Massachusetts and the Infrared Processing and Analysis Center/California Institute of Technology, funded by the National Aeronautics and Space Administration (NASA) and the National Science Foundation (NSF). We thank René Racine for refereeing this paper and for useful suggestions and Remi Soummer for suggesting the method of contour plots to present our detection limits. B. A. B. is supported by the NASA GSRP grant NNG04GN95H and NASA Origins grant NNG05GL71G. L. M. C. is supported by an NSF CAREER award and the NASA Origins of the Solar System program. E. L. N. is supported by a Michelson Fellowship.

REFERENCES

Alcala, J. M., Krautter, J., Schmitt, J. H. M. M., Covino, E., Wichmann, R., & Mundt, R. 1995, A&AS, 114, 109

Baraffe, I., Chabrier, G., Barman, T. S., Allard, F., & Hauschildt, P. H. 2003, A&A, 402, 701

Benedict, G. F., et al. 2006, AJ, 132, 2206

Berton, A., et al. 2006, PASP, 118, 1144

Bidelman, W. P. 1951, ApJ, 113, 304

Biller, B. A., Close, L. M., Lenzen, R., Brandner, W., McCarthy, D., Nielsen, E., Kellner, S., & Hartung, M. 2006a, in IAU Colloq. 200, Direct Imaging of Exoplanets: Science & Techniques, ed. C. Aime & F. Vakili (Cambridge: Cambridge Univ. Press), 571

Biller, B. A., Kasper, M., Close, L. M., Brandner, W., & Kellner, S. 2006b, ApJ, 641, L141

Biller, B. A., et al. 2006c, Proc. SPIE, 6272, 74

Boss, A. P. 2003, ApJ, 599, 577

Brandeker, A., Jayawardhana, R., Ivanov, V. D., & Kurtev, R. 2006, ApJ, 653, L61

Brandner, W., et al. 2000, AJ, 120, 950

Burgasser, A., et al. 2003, AJ, 125, 850

Burrows, A., Hubbard, W. B., Lunine, J. I., & Liebert, J. 2001, Rev. Mod. Phys., 73, 719

Burrows, A., Sudarsky, D., & Lunine, J. 2003, ApJ, 596, 587

Butler, R. P., et al. 2006, ApJ, 646, 505

Chauvin, G., Lagrange, A.-M., Dumas, C., Zuckerman, B., Mouillet, D., Song, I., Beuzit, J.-L., & Lowrance, P. 2005a, A&A, 438, L25

Chauvin, G., et al. 2005b, A&A, 438, L29

Christian, D. J., & Mathioudakis, M. 2002, AJ, 123, 2796

Close, L. M., Lenzen, R., Biller, B. A., Brandner, W., & Hartung, M. 2005a, in Science with Adaptive Optics, ed. W. Brandner & M. E. Kasper (Springer: Berlin), 136

Close, L. M., et al. 2005b, Nature, 433, 286

———. 2007a, ApJ, 660, 1492

———. 2007b, ApJ, 665, 736

Codona, J. L., & Angel, R. 2004, ApJ, 604, L117

Cowley, A. P., Hiltner, W. A., & Witt, A. N. 1967, AJ, 72, 1334

Cutispoto, G., Pallavicini, R., Kuerster, M., & Rodono, M. 1995, A&A, 297, 764

Cutri, R. M., et al. 2003, The IRSA 2MASS All Sky Catalog of Point Sources (Pasadena: NASA/IPAC)

Dohlen, K., et al. 2006, Proc. SPIE, 6269, 24

Favata, F., Barbera, M., Micela, G., & Sciortino, S. 1995, A&A, 295, 147

Favata, F., Micela, G., & Sciortino, S. 1997, A&A, 326, 647

Fischer, D. A., & Valenti, J. 2005, ApJ, 622, 1102

Geballe, T. R., et al. 2002, ApJ, 564, 466

Geissler, K., et al. 2007, A&A, 461, 665

Gliese, W., & Jahreiss, H. 1979, A&AS, 38, 423

———. 1991, in The Astronomical Data Center CD-ROM: Selected Astronomical Catalogs, Vol. I, ed. L. E. Brotzmann & S. E. Gesser (Greenbelt: Goddard Space Flight Center)

Gray, R. O., Corbally, C. J., Garrison, R. F., McFadden, M. T., Bubar, E. J., McGahee, C. E., O'Donoghue, A. A., & Knox, E. R. 2006, AJ, 132, 161

Gray, R. O., Corbally, C. J., Garrison, R. F., McFadden, M. T., & Robinson, P. E. 2003, AJ, 126, 2048

Hartung, M., et al. 2004, A&A, 421, L17

Hinkley, S., et al. 2007, ApJ, 654, 633

Houk, N. 1978, Michigan Catalogue of Two-Dimensional Spectral Types for the HD Stars, Vol. 2 (Ann Arbor: Univ. Michigan)

———. 1982, Michigan Catalogue of Two-Dimensional Spectral Types for the HD Stars, Vol. 3 (Ann Arbor: Univ. Michigan)

Houk, N., & Cowley, A. P. 1975, Michigan Catalogue of Two-Dimensional Spectral Types for the HD Stars, Vol. 1 (Ann Arbor: Univ. Michigan)

Houk, N., & Smith-Moore, M. 1988, Michigan Catalog of Two-Dimensional Spectral Types for the HD Stars, Vol. 4 (Ann Arbor: Univ. Michigan)

Ida, S., & Lin, D. N. C. 2005, ApJ, 626, 1045

Janson, M. et al. 2007, AJ, submitted

Kaisler, D., Zuckerman, B., & Becklin, E. 2003, in ASP Conf. Ser. 294, Scientific Frontiers in Research on Extrasolar Planets, ed. D. Deming & S. Seagar (San Francisco: ASP), 91

Kenworthy, M. A., Hinz, P. M., Angel, J. R. P., Heinze, A. N., & Sivanandam, S. 2006, Proc. SPIE, 6272, 104

Knapp, G. R., et al. 2004, AJ, 127, 3553

Lachaume, R., Dominik, C., Lanz, T., & Habing, H. J. 1999, A&A, 348, 897

Leaton, B. R., & Pagel, B. E. J. 1960, MNRAS, 120, 317

Lenzen, R., Close, L., Brandner, W., Biller, B., & Hartung, M. 2005, in Science with Adaptive Optics, ed. W. Brandner & M. E. Kasper (Springer: Berlin), 46

Lenzen, R., Close, L., Brandner, W., Hartung, M., & Biller, B. 2004, Proc. SPIE, 5492, 970

Lenzen, R., et al. 2003, Proc. SPIE, 4841, 944

Li, J. Z., & Hu, J. Y. 1998, A&AS, 132, 173

Liu, W., et al. 2007, ApJ, 658, 1164

Lowrance, P. J., et al. 2005, AJ, 130, 1845

Luhman, K. L., & Jayawardhana, R. 2002, ApJ, 566, 1132

Luhman, K. L., et al. 2006, ApJ, 649, 894

Macintosh, B., et al. 2006, Proc. SPIE, 6272, 18

Marley, M. S., Fortney, J. J., Hubickyj, O., Bodenheimer, P., & Lissauer, J. J. 2007, ApJ, 655, 541

Marois, C., Doyon, R., Racine, R., & Nadeau, D. 2000a, PASP, 112, 91

———. 2000b, Proc. SPIE, 4008, 788

Marois, C., Lafrenière, D., Doyon, R., Macintosh, B., & Nadeau, D. 2006, ApJ, 641, 556

Marois, C., et al. 2005, PASP, 117, 745

Masciadri, E., Mundt, R., Henning, T., Alvarez, C., & Barrado y Navascues, D. 2005, ApJ, 625, 1004

McCaughrean, M. J., Close, L. M., Scholz, R.-D., Lenzen, R., Biller, B., Brandner, W., Hartung, M., & Lodieu, N. 2004, A&A, 413, 1029

Metchev, S. A., & Hillenbrand, L. A. 2004, ApJ, 617, 1330

Meyer, M. R., Edwards, S., Hinkle, K. H., & Strom, S. E. 1998, ApJ, 508, 397

Mochnacki, S. W., et al. 2002, AJ, 124, 2868

Montes, D., López-Santiago, J., Gálvez, M. C., Fernández-Figueroa, M. J., De Castro, E., & Cornide, M. 2001, MNRAS, 328, 45

Mugrauer, M., & Neuhäuser, R. 2005, MNRAS, 361, L15

Nakajima, T., Oppenheimer, B. R., Kulkarni, S., Golimowski, D. A., Matthews, K., & Durrance, S. T. 1995, Nature, 378, 463

Neuhäuser, R., & Brandner, W. 1998, A&A, 330, L29

Nielsen, E. L., Close, L. M., & Biller, B. A. 2006, in IAU Colloq. 200, Direct Imaging of Exoplanets: Science & Techniques, ed. C. Aime & F. Vakili (Cambridge: Cambridge Univ. Press), 111

Nielsen, E. L., Close, L. M., Guirado, J. C., Biller, B. A., Lenzen, R., Brandner, W., Hartung, M., & Lidman, C. 2005, Astron. Nachr., 326, 1033

Nielsen, E., et al. 2007, ApJ, submitted

Noyes, R. W., Weiss, N. O., & Vaughan, A. H. 1984, ApJ, 287, 769

Perryman, M. A. C., et al. 1997, A&A, 323, 49

Racine, R., Walker, G. A. H., Nadeau, D., Doyon, R., & Marois, C. 1999, PASP, 111, 587

Randich, S., Gratton, R., & Pallavicini, R. 1993, A&A, 273, 194

Rousset, G., et al. 2003, Proc. SPIE, 4389, 140

Sozzetti, A., et al. 2006, A&A, 449, 417

Sparks, W. B., & Ford, H. C. 2002, ApJ, 578, 543

Tamura, M., & Lyu, A. 2006, in IAU Colloq. 200, Direct Imaging of Exoplanets: Science & Techniques, ed. C. Aime & F. Vakili (Cambridge: Cambridge Univ. Press), 323

Thatte, N., et al. 2007, MNRAS, 378, 1229

Torres, G., Stefanik, R., Latham, D., & Mazeh, T. 1995, ApJ, 452, 870

Trauger, J. T., et al. 2004, Proc. SPIE, 5487, 1330

Wichmann, R., Schmitt, J. H. M. M., & Hubrig, S. 2003, A&A, 400, 293

Wright, J. T., Butler, R. P., Marcy, G. W., Vogt, S. S., Fischer, D. A., Rinney, C. G., & Jones, H. R. A. 2005, in Protostars and Planets V, ed. V. Mannings et al. (Houston: Lunar and Planetary Institute), 8605

Wright, J. T., Marcy, G. W., Butler, R. P., & Vogt, S. S. 2004, ApJS, 152, 261

Zuckerman, B., & Song, I. 2004, ARA&A, 42, 685

Zuckerman, B., Song, I., Bessell, M. S., & Webb, R. A. 2001a, ApJ, 562, L87

Zuckerman, B., Webb, R. A., Schwartz, M., & Becklin, E. E. 2001b, ApJ, 549, L233